

This is an Open Access document downloaded from ORCA, Cardiff University's institutional repository: <https://orca.cardiff.ac.uk/id/eprint/174751/>

This is the author's version of a work that was submitted to / accepted for publication.

Citation for final published version:

Sayadi Moghadam, Sina , Mihai, Iulia and Jefferson, Anthony 2024. Rate dependent self-healing model for cementitious materials. *International Journal of Solids and Structures* , 113196.
10.1016/j.ijsolstr.2024.113196

Publishers page: <https://doi.org/10.1016/j.ijsolstr.2024.113196>

Please note:

Changes made as a result of publishing processes such as copy-editing, formatting and page numbers may not be reflected in this version. For the definitive version of this publication, please refer to the published source. You are advised to consult the publisher's version if you wish to cite this paper.

This version is being made available in accordance with publisher policies. See <http://orca.cf.ac.uk/policies.html> for usage policies. Copyright and moral rights for publications made available in ORCA are retained by the copyright holders.



1 Rate dependent self-healing model for cementitious materials

2 Sina Sayadi*, Iulia Mihai, Anthony Jefferson

3 *School of Engineering, Cardiff University, Queen's Buildings, The Parade, Cardiff, CF24*
4 *3AA Wales, United Kingdom*

5 **Corresponding author: Sayadimoghams@cardiff.ac.uk*

6 **Abstract**

7 A new micromechanics-based constitutive model for self-healing cementitious materials
8 is proposed. The model is aimed at self-healing materials with distributed healing
9 mechanisms, such as materials with embedded microcapsules and enhanced
10 autogenous healing capabilities. The model considers anisotropic microcracking and
11 time-dependent healing. In contrast to many existing models for self-healing
12 cementitious materials, the new approach imposes no limitations on the number or
13 timing of microcracking or healing events that can be simulated. The formulation ensures
14 that the simulation of microcracking and healing is always consistent with the second
15 law of thermodynamics. The model is implemented in a three-dimensional nonlinear
16 finite element code that allows structural elements formed from self-healing materials
17 to be simulated. A series of single-point simulations illustrate the versatility of the model.
18 The experiments considered with the model encompass a set of cylindrical specimens
19 formed from concrete with embedded microcapsules containing sodium silicate, and a
20 notched beam test series that examined the self-healing potential of concrete formed
21 with a crystalline admixture. The validations show that the model can capture the

22 characteristic mechanical behaviour of these structural elements with good engineering
23 accuracy.

24 **Keywords:** Micromechanical model, rate-dependent healing, finite element analysis,
25 self-healing.

26 **1 Introduction**

27 There has been strong interest in the development of self-healing cementitious materials
28 (SHCM) over the last two decades due to the need to improve the durability and
29 resilience of civil engineering structures. The development, design and assessment of
30 these SHCM structures requires accurate and robust models that can capture their
31 fundamental behaviour, particularly in the absence of design codes of practice. The
32 earliest models for self-healing systems simulated wound healing. These models (Arnold
33 & Adam 1999; Vermolen, *et al.* 2006) considered a diffusion process to capture healing
34 growth within designated wound layers. Although the development of biomimetic
35 construction materials is inspired by natural processes in biological systems, the
36 underlying cracking and healing mechanisms differ significantly from those of their
37 organic counterparts. Self-healing in cementitious materials involves a series of physical
38 and chemical processes (Shields *et al.* 2021; Van Tittelboom & De Belie 2013) that
39 include: i) mechanical cracking and healing, ii) fluid and heat transport, and iii) chemical
40 reactions and the associated curing of healing agents.

41 Various approaches have been explored to capture the behaviour of SCHMs in cracking-
42 healing cycles, and several coupled models have been presented that can simulate these
43 processes (Jefferson *et al.* 2018). In recent studies, morphological methods have been
44 employed to establish a mathematical relationship between healing mechanisms and

45 post-healed mechanical properties (Lee & Anthony 2023; Ponnusami *et al.* 2019; Zhou
46 *et al.* 2017). However, most existing models are either fully or semi-empirical in nature
47 and require considerable experimental data to calibrate their response for a particular
48 SCHM. This implies that these models are only valid within the data range considered.

49 In general, two general approaches have been employed to simulate mechanical self-
50 healing processes; namely, the discrete crack approach (Al-Rub 2016; Caggiano *et al.*
51 2017; Cibelli *et al.* 2022; Freeman *et al.* 2020; Jefferson & Freeman 2022) and the
52 smeared crack approach (Davies & Jefferson 2017; Dutta & Kishen 2019; Han *et al.*
53 2021a; James *et al.* 2014; Zhou *et al.* 2016; Zhu *et al.* 2015, 2016).

54 Several constitutive models have employed Continuum Damage Healing Mechanics
55 (CDHM) as a modelling framework (Oucif & Mauludin 2018). In this approach, the
56 evolution of healing is linked to the degree of damage by introducing a healing variable
57 (scalar or tensor) that describes the proportion of the effective damage area that has
58 healed. This progresses according to a phenomenological healing evolution function
59 (Abu Al-Rub & Darabi 2012; Darabi *et al.* 2012).

60 For ductile materials, the elastoplastic constitutive formulation proposed by Barbero
61 *et al.* (2005) has been used by several authors (Voyiadjis *et al.* 2011). This formulation
62 uses the concept of elastic strain energy equivalence to derive damage-healing tensors.
63 This idea was subsequently extended by Subramanian & Mulay (2022) to encompass self-
64 healing in shape memory polymers.

65 Several investigators have shown that micromechanics-based models are able to
66 describe the behavioural characteristics of multiphase quasi-brittle materials (Monchiet
67 *et al.* 2012). In the case of cementitious materials, a micromechanical formulation has

68 been employed to represent various mechanisms and processes, including the hydration
69 reactions of distinct phases within a cement paste (Königsberger *et al.* 2020; Pichler *et*
70 *al.* 2013; Pichler & Hellmich 2011). The micromechanics approach has also been used to
71 simulate the effects of microcracks on the overall response of cement paste arising from
72 early-age cracking and/or mechanical loading (Dutta & Kishen 2019; Pensée *et al.* 2002;
73 Pichler *et al.* 2007).

74 Employing micromechanics formulations to represent cracking in quasi-brittle
75 composite materials has also enabled the development of mechanistic models suitable
76 for self-healing applications in these materials. Chen *et al.* 2022; Zhu & Arson 2014; Zhu
77 *et al.* 2015, 2016 employed a 2D micromechanical framework to simulate the behaviour
78 of microencapsulation self-healing systems under tensile and compressive loads. They
79 used classical fracture mechanics to establish a microcracking evolution relationship and
80 derived a compliance tensor for the healed material. Subsequently, Chen *et al.* (2022)
81 considered aligned penny-shaped microcracks to evaluate the overall compliance matrix
82 for concrete after healing as a function of the crack healing ratio. In their formulation,
83 crystallization reaction kinetics was used to compute the degree of healing.

84 In another significant study, Davies and Jefferson (2017) developed a 3D model aimed
85 at describing autogenous self-healing in cementitious materials. The model is able to
86 simulate anisotropic microcracking and healing, but healing was considered to be
87 instantaneous and thus the model did not consider the time-dependent nature of
88 healing. The majority of these models considered single healing events although some
89 also incorporated re-damage in their mathematical formulations (Oucif & Mauludin
90 2018).

91 More recently, Han *et al.* 2021a, 2021b proposed a micromechanical formulation to
92 simulate the mechanical behaviour of self-healing concrete. Their approach adopted
93 linear fracture mechanics criteria for both damage initiation and evolution. In a broader
94 context, Sanz-Herrera *et al.* (2019) introduced a comprehensive framework that
95 considers multiple healing cycles in self-healing materials, based on the assumption that
96 each healing step is initiated under fully unloaded conditions.

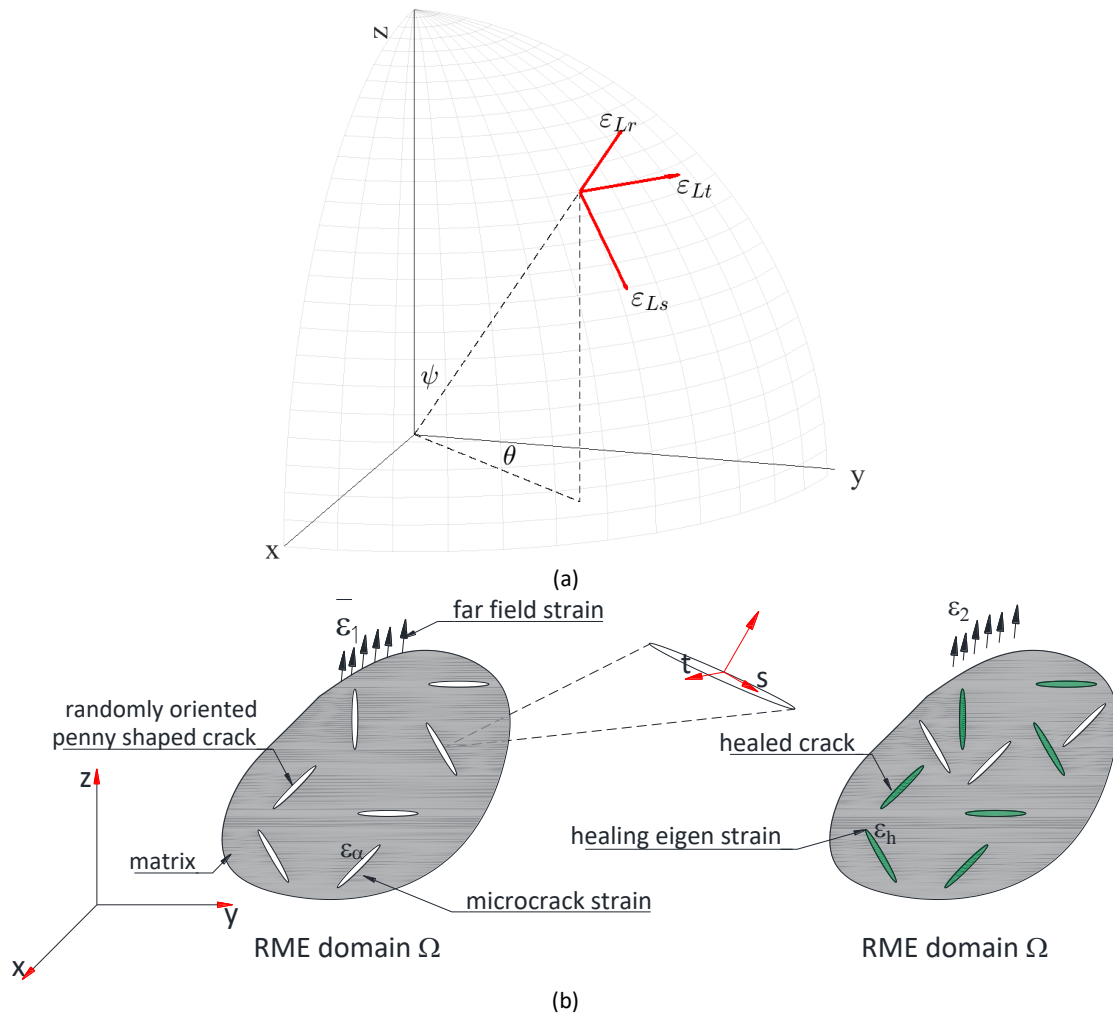
97 In this paper, a micromechanics-based constitutive model for SHCMs is presented,
98 which incorporates directional microcracking and rate-dependent healing. The primary
99 novel aspect of the work is the introduction of rate dependent healing into a
100 micromechanical model that does not have restrictions on the number of healing cycles,
101 the strain conditions under which healing takes place, and which also allows
102 simultaneous microcracking and healing. This builds on previous work by the authors'
103 team on micromechanical models for cementitious composites (Mihai and Jefferson,
104 2011) and -specifically- on the work of Davies and Jefferson (2017) on a micromechanical
105 model for self-healing cementitious materials, which had considerable restrictions, as
106 explained above. This research also draws upon the theory developed for a discrete
107 damage-healing model that was applied to elements with embedded strong
108 discontinuities (Jefferson and Freeman, 2023). A second, more arcane, contribution
109 relates to the strict enforcement of the condition that there should be zero-stress change
110 during an increment of pure healing. This condition is important for ensuring that
111 spurious energy is not created during healing. The way that this condition was
112 considered in Davies and Jefferson's model is inadequate for the more general
113 microcracking-healing scenarios of this paper.

114 The layout of the remainder of this paper is as follows; section 2 presents the basic
115 model theory followed by a description of its numerical implementation; in section 3 the
116 constitutive response predicted by the model is illustrated using a series of single
117 material point simulations, and this is followed by the presentation of a boundary value
118 problem in section 4. Finally, the main conclusions from the work are drawn in section
119 5. In this paper, the only damage considered is mechanical loss of strength and stiffness
120 due to microcracking.

121 **2 Constitutive formulation for microcracking and healing**

122 The main concepts of the constitutive model are presented in Figure 1. The cementitious
123 composite is modelled as an elastic solid containing a series of randomly distributed
124 circular microcracks which can have any orientation, defined by ψ and θ (see Figure 1a).
125 Each direction has a set of local unit vectors, with the vector \mathbf{r} being normal to the
126 microcrack plane, and \mathbf{s} and \mathbf{t} being in-plane vectors. The model simulates healing using
127 time dependent variables to describe the repair of these directional microcracks (see
128 Figure 1b). In addition, a set of healing strain tensors are introduced for every local
129 microcracking direction to simulate the permanent strains that occur when healing agent
130 cures in open microcracks. The formulation ensures that no spurious energy is created
131 when healing occurs.

132



133 Figure 1. Schematic representation of RME. a) Coordinate system: b) illustration of
 134 microcracked (left) and partially healed (right), material states.

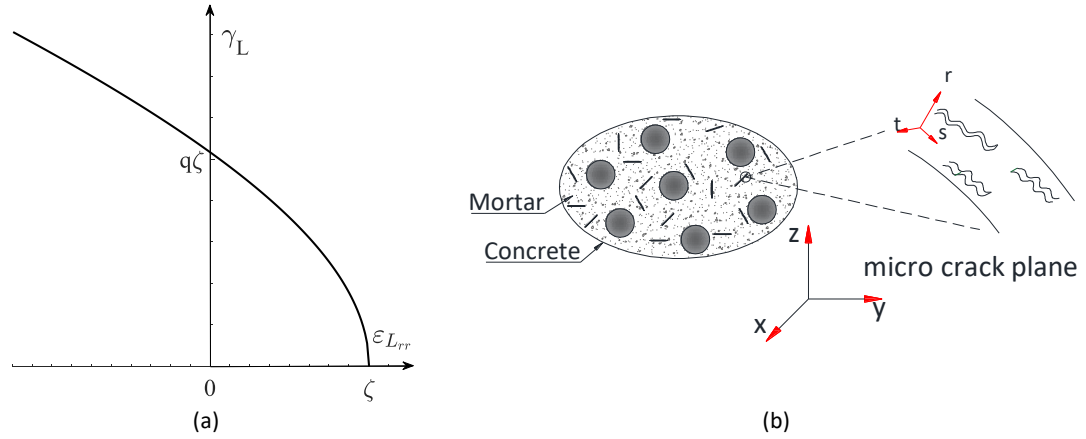
135 **2.1 Constitutive equations for a model with directional microcracking**

136 The model draws on a series of previous micromechanics-based constitutive
 137 formulations for cementitious materials (Davies & Jefferson, 2017; Jefferson & Bennett
 138 2007; Jefferson and Bennett, 2010; Mihai & Jefferson 2011). The essential equations
 139 from the underlying micromechanical model, required for the derivation of the new
 140 healing model, are summarised in Table 1. In the Table, 'total' refers stress, strain and
 141 constitutive tensors in Cartesian axes, and 'local' refers to directional terms, which are
 142 either integrated to give the total terms (see equation 2) or transformed from total
 143 tensors (see equations 8 and 9).

Table 1. Summary of equations from the underlying microcracking model.

Equation	Number	Description (Jefferson and Bennett, 2007 & 2010)
$\boldsymbol{\sigma} = \mathbf{D} : (\boldsymbol{\varepsilon} - \boldsymbol{\varepsilon}_{\text{add}})$	(1)	Total constitutive relationship.
$\boldsymbol{\varepsilon}_{\text{add}} = \frac{1}{2\pi} \oint_S \mathbf{N}_\varepsilon : \boldsymbol{\varepsilon}_\alpha \, dS$	(2)	Total added strain tensor obtained by integrating the local added strain tensor (which varies with direction) over a hemisphere.
$\boldsymbol{\varepsilon}_\alpha = \left(\frac{\omega}{1-\omega}\right) \mathbf{C}_L : \mathbf{s}$	(3)	Local added strain tensor in terms of the local stress, elastic compliance and local microcracking variable.
$\mathbf{s} = (1 - \omega) \mathbf{D}_L : \boldsymbol{\varepsilon}_L$	(4)	Local constitutive relationship in terms of the local strain (sum of elastic and added local strains) and local elasticity tensor.
$F_\zeta(\boldsymbol{\varepsilon}_L, \zeta) = \zeta_{ef}(\boldsymbol{\varepsilon}_L) - \zeta = 0$ subject to	(5)	Microcracking function in terms of the local microcracking strain (ζ_{ef}) (see footnotes) and the local microcracking strain parameter.
$F_\zeta \leq 0; \dot{\zeta} \geq 0; F_\zeta \dot{\zeta} = 0$	(6)	$F_\zeta(\boldsymbol{\varepsilon}_L, \zeta)$ is subject to the Karush–Kuhn–Tucker conditions, equation (6), which are applied to equation (5) such that local strains remain on the microcracking surface when local microcracking is active in a particular direction (Mihai & Jefferson, 2012). In the present case, this involves updating ζ to the value of $\zeta_{ef}(\boldsymbol{\varepsilon}_L)$, if the latter exceeds the value of the former from the last converged state.
$\omega(\zeta) = 1 - \frac{\varepsilon_t}{\zeta} e^{-c \left(\frac{\zeta - \varepsilon_t}{\varepsilon_0 - \varepsilon_t}\right)}$	(7)	Local microcracking variable in terms of the microcracking strain parameter.
$\mathbf{s} = \mathbf{N} : \boldsymbol{\sigma}$	(8)	Transformations for local stress and strain from their total counterparts.
$\boldsymbol{\varepsilon}_L = \mathbf{N}_\varepsilon^T : \boldsymbol{\varepsilon}$	(9)	
<p>Notation and notes.</p> <p>$\boldsymbol{\varepsilon}_{\text{add}}$ is the overall additional strain tensor due to microcracking, $\boldsymbol{\sigma}$ and $\boldsymbol{\varepsilon}$ are the total stress and strain tensors respectively, \mathbf{D} is the elasticity tensor, \mathbf{N} is the stress transformation tensor, \mathbf{N}', in matrix terms, is equal to \mathbf{N}^T, \mathbf{N}_ε is a strain transformation tensor, $\boldsymbol{\varepsilon}_\alpha$ is the local added strain tensor, S denotes the surface of a unit hemisphere, ω is the directional microcracking variable, \mathbf{C}_L is the local elastic compliance tensor, \mathbf{s} is the local stress tensor, $\mathbf{D}_L = \mathbf{C}_L^{-1}$ is the local elasticity tensor, $\boldsymbol{\varepsilon}_L$ is a local strain tensor that comprises the sum of the added ($\boldsymbol{\varepsilon}_\alpha$) and the elastic ($\boldsymbol{\varepsilon}_{Le}$) local strains, F_ζ is the microcracking function (also known as the local microcracking strain surface), ζ_{ef} is the effective microcracking strain (see below), ζ is the microcracking strain parameter, c is the microcrack evolution constant, $\varepsilon_0 = u_0/\ell_e$ is the strain at the fully microcracked state, u_0 is displacement at the end of the softening curve, ℓ_e is the finite element characteristic length, $\varepsilon_t = f_t/E$, f_t is the uniaxial tensile stress at which microcracking initiates and E is Young's modulus of the cementitious matrix material. Local tensors are expressed in a reduced vector or matrix form in which only those terms that can be non-zero are included e.g. $\mathbf{s} = [s_{rr} \ s_{rs} \ s_{rt}]^T$.</p> <p>$\zeta_{ef}(\boldsymbol{\varepsilon}_L) = \left(\frac{\varepsilon_{Lrr}}{2} \left(1 + \left(\frac{\mu}{q}\right)^2\right) + \frac{1}{2q^2} \sqrt{\varepsilon_{Lrr}^2 (q^2 - \mu^2)^2 + 4q^2 \gamma^2}\right)$, in which $\mu = \frac{\mu_s E}{G}$, $\gamma = \sqrt{\varepsilon_{Lrs}^2 + \varepsilon_{Lrt}^2}$, $q = \frac{q_s E}{G}$, μ_s is an internal friction parameter and q_s is the ratio of interface shear strength to matrix tensile strength.</p>		

146 Figure 2a illustrates the microcracking strain surface (equation 5) and Figure 2b shows a
 147 set of parallel microcracks in the cementitious composite.



148 Figure 2. Microcracking strain surface, b) parallel set of microcracks

149 2.2 Derivation of model constitutive equations

150 Healing is simulated by the addition of a new term to the right-hand-side of the local
 151 constitutive equation (4) such that the local stress in an RME comprises two components,
 152 the first term representing the proportion of un-microcracked material, and the second
 153 term giving the proportion of healed – re-microcracked material. The resulting equation
 154 is as follows:

$$155 \mathbf{s}_{Lh} = (1 - \omega) \mathbf{D}_L : \boldsymbol{\varepsilon}_L + h_v (1 - \omega_h) \mathbf{D}_{Lh} : (\boldsymbol{\varepsilon}_L - \boldsymbol{\varepsilon}_h) \quad (10)$$

156 where \mathbf{s}_{Lh} , which replaces \mathbf{s} used in equation 4, is the local stress tensor allowing for
 157 any healing, and \mathbf{D}_{Lh} the local elasticity matrix of the healed material, $\boldsymbol{\varepsilon}_h$ is the healing
 158 strain and ω_h is the re-microcracking variable. It is noted that
 159 \mathbf{s}_{Lh} , ω , $\boldsymbol{\varepsilon}_L$, ω_h , $\boldsymbol{\varepsilon}_L$ & $\boldsymbol{\varepsilon}_h$ all vary with time (t) and with direction (ψ and θ), but these
 dependencies have been omitted for clarity of presentation.

160 The healing variable ($h_v \in [0, \omega]$) represents the proportion of microcracked material
 161 that is healed at a given time in the absence of re-microcracking. More specifically, h_v is

162 equal to the maximum healing front position, in increasing microcracking terms, in a
 163 given direction. The evolution of h_v for the present micromechanical model is explained
 164 in section 2.3. The model accounts for re-microcracking of healed material by employing
 165 a second microcracking variable ($\omega_h \in [0,1]$), which gives the proportion of h_v that has
 166 re-microcracked. When healed material re-microcracks, ω_h evolves according to
 167 equations (11) and (12), which are the healing counterparts to equations (7) and (5)
 168 respectively.

$$169 \quad \omega_h(\zeta_h) = 1 - \frac{\varepsilon_t}{\zeta_h} e^{-c \left(\frac{\zeta_h - \varepsilon_{ht}}{\varepsilon_{h0} - \varepsilon_{ht}} \right)} \quad (11)$$

$$170 \quad F_{\zeta_h}(\varepsilon_L, \varepsilon_h, \zeta) = \zeta_{hef}(\varepsilon_L - \varepsilon_h) - \zeta_h = 0 \quad (12)$$

171 where $\zeta_{hef}, \zeta_h, \varepsilon_{h0}$ & ε_{ht} are the healing counterparts to the microcracking
 172 function/parameters $\zeta_{ef}, \zeta, \varepsilon_0$ & ε_t . It is noted that when re-healing occurs, ω_h reduces, as
 173 explained below.

174 The general form of equation (10) is similar to the local constitutive equation employed
 175 by Davies and Jefferson (2017), but the meaning of the healing and re-microcracking
 176 variables and the way that they are updated are quite different. This is because the
 177 model by Davies and Jefferson only allowed one healing and one re-microcracking event.
 178 Furthermore, in their model, healing terms did not evolve over time.

179 When healing agent cures in an open microcrack, there is a moment in time when solid
 180 material first bridges between the opposing crack faces. This is when mechanical healing
 181 of the crack commences, and it is assumed that this bridging material is stress free at the
 182 time of formation. This 'stress free at formation' condition is assumed to apply to every
 183 new increment of bridging material. This assumption is not only consistent with

184 experimental data (Selvarjoo et al. 2020), but also ensures that the simulation of healing
185 does not create spurious energy and therefore does not violate the second law of
186 thermodynamics. Expanding on this issue; when healing is simulated, the stiffness of the
187 material increases. Thus, if the strain remained constant, the stress and the strain energy
188 would increase. This would violate the second law unless the increase in strain energy
189 was matched by the release of thermal-chemical energy. Since there is no evidence that
190 the stress rises during healing, the surest way to ensure that the model satisfies
191 thermodynamics principles is to introduce a healing strain (ϵ_h) that evolves such that the
192 stress does not change due to healing alone. Furthermore, this strain simulates the
193 permanent strains associated with solidified healing agent, which prevents microcracks
194 from fully closing. This permanent strain is evident in experiments in which healing has
195 occurred in open cracks (Selvarajoo et al., 2020). A mathematical treatment of this issue
196 may be found in Appendix B of Jefferson and Freeman (2022), in the context of a discrete
197 cracking model. The method used to update ϵ_h is discussed below.

198 The derivation now proceeds by determining the total inelastic strain tensor for each
199 direction, which is the equivalent of equation (3). This is accomplished by rearranging
200 equation (10) to give the local strain, as follows:

$$\epsilon_L = [(1 - \omega)\mathbf{D}_L + h_v(1 - \omega_h)\mathbf{D}_{Lh}]^{-1}: [\mathbf{s}_{Lh} + h_v(1 - \omega_h)\mathbf{D}_{Lh}: \epsilon_h] \quad (13)$$

201 Then, the local inelastic strain tensor (ϵ_α) is found by removing the elastic component
202 of strain from ϵ_L (i.e. $\epsilon_\alpha = \epsilon_L - \epsilon_{Le}$, where $\epsilon_{Le} = \mathbf{C}_L: \mathbf{s}_{Lh}$). Thus, from (13), the
203 additional local inelastic strain is given by:

$$\epsilon_\alpha = [(1 - \omega)\mathbf{D}_L + h_v(1 - \omega_h)\mathbf{D}_{Lh}]^{-1}: [\mathbf{s}_{Lh} + h_v(1 - \omega_h)\mathbf{D}_{Lh}: \epsilon_h] - \mathbf{C}_L: \mathbf{s}_{Lh} \quad (14)$$

204 which is rearranged to group local stress and healing strain terms, as follows:

$$\boldsymbol{\varepsilon}_\alpha = [[(1-\omega)\mathbf{D}_L + h_v(1-\omega_h)\mathbf{D}_{Lh}]^{-1} - \mathbf{C}_L] : \mathbf{s}_{Lh} + \left[\frac{(1-\omega)}{h_v(1-\omega_h)} \mathbf{C}_{Lh} \cdot \mathbf{D}_L + \mathbf{I}^{2s} \right]^{-1} : \boldsymbol{\varepsilon}_h \quad (15)$$

205 where \mathbf{I}^{2s} is the second order identity tensor, and $\mathbf{C}_{Lh} = \mathbf{D}_{Lh}^{-1}$.

206 The total inelastic strain tensor is obtained by integrating the contributions from (15)
 207 around a hemi-sphere, in the same way that the equivalent term was obtain in equation
 208 (2), giving the following:

$$\boldsymbol{\varepsilon}_{\text{add}} = \frac{1}{2\pi} \oint_S \mathbf{N}_\varepsilon : ([[(1-\omega)\mathbf{D}_L + h_v(1-\omega_h)\mathbf{D}_{Lh}]^{-1} - \mathbf{C}_L] : \mathbf{s}_{Lh} + \left[\frac{(1-\omega)}{h_v(1-\omega_h)} \mathbf{C}_{Lh} \cdot \mathbf{D}_L + \mathbf{I}^{2s} \right]^{-1} : \boldsymbol{\varepsilon}_h) dS \quad (16)$$

211 The two components of equation (16) are now separated, as follows:

$$\boldsymbol{\varepsilon}_{\text{at}} = \frac{1}{2\pi} \oint_S \mathbf{N}_\varepsilon : [[(1-\omega)\mathbf{D}_L + h_v(1-\omega_h)\mathbf{D}_{Lh}]^{-1} - \mathbf{C}_L] : \mathbf{s}_{Lh} \quad dS \quad (17)$$

$$\boldsymbol{\varepsilon}_{\text{ah}} = \frac{1}{2\pi} \oint_S \mathbf{N}_\varepsilon : \left[\frac{(1-\omega)}{h_v(1-\omega_h)} \mathbf{C}_{Lh} \cdot \mathbf{D}_L + \mathbf{I}^{2s} \right]^{-1} : \boldsymbol{\varepsilon}_h \quad dS \quad (18)$$

212 The first term ($\boldsymbol{\varepsilon}_{\text{at}}$) gives the inelastic strain induced by the local stresses and the second
 213 term gives the total permanent strain due to cured healing agent.

214 The method used to evaluate $\boldsymbol{\varepsilon}_h$ is described in Section 2.3 and expanded upon in
 215 Appendix B. The latter accounts for interactions between healed microcracks in different
 216 directions, which were not considered in the method proposed by Davies and Jefferson
 217 (2017).

218 The relationship between the total stress and strain tensors is derived by replacing $\boldsymbol{\varepsilon}_{\text{add}}$
 219 in equation (1) with the two components from equations (17) and (18), as follows:

$$\boldsymbol{\sigma} = \mathbf{D} : (\boldsymbol{\varepsilon} - \boldsymbol{\varepsilon}_{\text{at}} - \boldsymbol{\varepsilon}_{\text{ah}}) \quad (19)$$

221 The final steps in this derivation involve using equations (17) and (18) in equation (19),
 222 employing the static constraint (equation 20) and rearranging to obtain equation (21).

$$\mathbf{s}_{Lh} = \mathbf{N} : \boldsymbol{\sigma} \quad (20)$$

223

$$\boldsymbol{\sigma} = \mathbf{D}_{sech} : (\boldsymbol{\varepsilon} - \boldsymbol{\varepsilon}_{ah}) \quad (21)$$

224

where \mathbf{D}_{sech} is the equivalent secant stiffness tensor, as given below.

$$\mathbf{D}_{sech} = (\mathbf{I}^{4s} + \frac{\mathbf{D}}{2\pi} \cdot \left(\frac{1}{2\pi} \oint_S \mathbf{N}_\varepsilon \cdot [\mathbf{A}^{-1} - \mathbf{C}_L] \cdot \mathbf{N} \, dS \right)^{-1} \cdot \mathbf{D}) \quad (22)$$

225

where \mathbf{I}^{4s} is fourth order identity tensor and $\mathbf{A} = [(1 - \omega)\mathbf{D}_L + h_v(1 - \omega_h)\mathbf{D}_{Lh}]$.

226

2.3 Time dependent healing evolution

227

In this section, the method used to simulate the evolution of the healing variables is

228

explained. This starts with a consideration of the relative proportion of material available

229

to heal at a given time t , which is denoted by $a(t)$. It is assumed that healing agent is

230

supplied instantaneously to any new microcracks and, thus, $a(t)$ increases at the same

231

rate as $\omega(t)$, as follows:

$$\dot{a}(t) = \dot{\omega}(t) \quad (23)$$

232

in which the superior dot denotes the time derivative.

233

Healing occurs by healing-agent curing in microcracks. The function used to simulate

234

the evolution of the degree of cure ($\phi \in [0,1]$) is taken from Freeman & Jefferson

235

(2022a, 2023), as follows:

$$\phi(t) = (1 - e^{-t_c/\tau}) \quad (24)$$

236

where τ is the curing time parameter, which depends on the chemical properties of

237

the healing agent and the current curing time ($t_c = t - t_{c0}$).

238 With these assumptions, and in the absence of re-microcracking, the virgin healing
 239 variable at time t is given by the following convolutional integral:

$$h_v(t) = \phi_{he} \int_{s=t_{c0}}^t \frac{\partial a(s)}{\partial s} (1 - e^{-\frac{t-s}{\tau}}) ds \quad (25)$$

240 where ϕ_{he} is a healing efficiency parameter.

241 The assumption that the degree of cure matches the degree of healing is different from
 242 that used in the macrocrack healing model of Jefferson and Freeman (2022), in which
 243 healing was computed from the overlap of curing fronts within a macro-crack. However,
 244 in microcracks with relatively small crack opening displacements, the degree of healing
 245 may be equated directly to ϕ .

246 Re-healing is simulated by a reduction in the re-microcracking variable (ω_h) such that
 247 the total proportion of healed material (h) at time t is:

$$h(t) = h_v(t)(1 - \omega_h(t)) \quad (26)$$

248 The relative proportion of material available for re-healing (a_r) is given by:

$$a_r(t) = h_v(t)\omega_h(t) \quad (27)$$

250 The re-healing variable is then obtained from:

$$h_r(t) = \phi_{he} \int_{t_{hr}}^t \frac{\partial a_r}{\partial s} (1 - e^{-t/\tau}) ds \quad (28)$$

251 where t_{hr} is the re-healing activation time.

252 The process of updating ω_h is best explained by considering a finite healing period from
 253 time t to $t + \Delta t_h$ and exploring the changes in the healing variables over that period.

254 The increment of virgin healing Δh_v is computed from equation (29) using equation (25),

255 the amount of re-healing Δh_r from equation (30) using equation (28), and ω_h by applying
 256 the healing increment to equation (26) to obtain equation (31) and rearranging to give
 257 equation (32):

$$258 \quad \Delta h_v = h_v(t + \Delta t_h) - h_v(t) \quad (29)$$

$$260 \quad \Delta h_r = h_r(t + \Delta t_h) - h_r(t) \quad (30)$$

$$261 \quad (1 - \omega_h(t + \Delta t_h))h_v(t + \Delta t_h) = (1 - \omega_h(t))h_v(t) + \Delta h_v + \Delta h_r \quad (31)$$

$$262 \quad \omega_h(t + \Delta t_h) = 1 - \frac{(1 - \omega_h(t))h_v(t) + \Delta h_v + \Delta h_r}{h_v(t + \Delta t_h)} \quad (32)$$

263 The representation of healing, re-microcracking and re-healing by equation (26)
 264 implies a homogenisation of material states across an RME. This is because the model
 265 does not track each separate directional component of micro-cracked and healed
 266 material that forms at a particular time; rather, these are grouped together and
 267 represented by a single virgin healing variable, a single microcracking variable and a
 268 single healing strain tensor (ϵ_h) for each microcracking direction. These microcracking
 269 and healing processes are illustrated in Figure 3.

270 The next healing component that needs to be considered is the healing strain. As
 271 discussed in Section 2.2, the condition used to compute ϵ_h is that the state of stress
 272 should not change when healing alone occurs. If the local stress is considered and there
 273 is no change in either ω or ϵ_L over the healing increment, then the zero change in the
 274 local stress condition may be written as follows:

$$275 \quad \Delta \mathbf{s}_{Lh} = h_v(t + \Delta t_h)(1 - \omega_h(t + \Delta t_h))\mathbf{D}_{Lh} : (\epsilon_L - \epsilon_h(t + \Delta t_h)) = h_v(t)(1 - \omega_{h_p})\mathbf{D}_{Lh} : (\epsilon_L - \epsilon_h(t)) = \mathbf{0} \quad (33)$$

276 where ω_{h_p} is the microcracking variable at the start of the healing sub-step.

277 Then, the change in the value of ϵ_h at the end of the healing increment may be deduced
 278 to be:

$$279 \quad \epsilon_h(t + \Delta t_h) = \frac{h_v(t + \Delta t_h)(1 - \omega_h(t + \Delta t_h))\epsilon_L - h_v(t)(1 - \omega_{hp})(\epsilon_L - \epsilon_h(t))}{h_v(t + \Delta t_h)(1 - \omega_h(t + \Delta t_h))} \quad (34)$$

280 This update ignores the interaction between local directions and means that if ϵ_h from
 281 equation (34) were to be used directly in equation (18) the condition that the total stress
 282 remains constant over a healing increment would not be guaranteed. The solution to this
 283 problem involves the introduction of an interaction factor (α_j) for each microcracking
 284 direction (j), as explained in Appendix B. These interaction factors modify the
 285 contribution of each local healing strain tensor (ϵ_h) to the total healing tensor ϵ_{ah} . The
 286 modified ϵ_{ah} tensor is denoted ϵ_{Gh} (see equation B.8) and is given by:

$$287 \quad \epsilon_{Gh} = \mathbf{C} \boldsymbol{\alpha} \epsilon_h \quad (35)$$

288 The expression in equation (35) then replaces ϵ_{ah} in equation (21), as follows:

$$289 \quad \boldsymbol{\sigma} = \mathbf{D}_{sech} : (\boldsymbol{\epsilon} - \epsilon_{Gh}) \quad (36)$$

290 The final aspect of the management of the healing variables is the update of the
 291 healing strain parameter (ζ_h) to account for the change in ω_h due to healing. This is
 292 obtained by solving the following nonlinear equation which is derived by equating
 293 $\omega_h(t + \Delta t_h)$ from equation (32) to the expression for ω_h given in equation (11), as follows:

$$294 \quad \text{solve } \omega_h(t + \Delta t_h) - \left(1 - \frac{\epsilon_t}{\zeta_h} e^{-c \left(\frac{\zeta_h(t + \Delta t_h) - \epsilon_{ht}}{\epsilon_{h0} - \epsilon_{ht}} \right)} \right) = 0 \quad \text{for } \zeta_h(t + \Delta t_h) \quad (37)$$

295

296 2.4 Update algorithm for healing variables

297 The numerical solutions used for the above equations are now considered. Firstly, h_v
298 and h_r are defined by the convolution integrals given in equations (25) and (28)
299 respectively, which may be solved conveniently by using a standard two-level recursive
300 scheme (Simo and Hughes, 1998; Mergheim and Steinmann, 2013). The resulting
301 expressions for h_v and h_r are as follows, noting that times t and $t + \Delta t_h$ are now
302 denoted by subscripts i and $i+1$ respectively:

$$h_{v_{i+1}} = h_{v_i} e^{-\frac{\Delta t_h}{\tau}} + \phi_{he} a_{i+1} (1 - e^{-\frac{\Delta t_h}{\tau}}) \quad (38)$$

$$h_{r_{i+1}} = h_{r_i} e^{-\frac{\Delta t_h}{\tau}} + \phi_{he} a_{r_{i+1}} \left(1 - e^{-\frac{\Delta t_h}{\tau}}\right) \quad (39)$$

303 Each time step is sub-divided into a microcracking sub-step and a healing sub-step.
304 The solution is quasi-static such that no inertia terms are included, and it is assumed that
305 any changes to the microcracking field occur instantaneously at the start of each time
306 step. Healing is then considered to occur over the time step, starting from the current
307 state of microcracking. Thus, the healing sub-step (Δt_h) is the same duration as the
308 overall time step (Δt).

309 The algorithm developed for computing the stress and updating the microcracking and
310 healing variables at a particular timestep is given in Algorithm box 1. The primary
311 directional microcracking and healing variables/tensors to be updated are
312 $\zeta, \zeta_h, \omega_h, h_v$ and ε_h . The dependent variables include ω & h_r . It is noted that ω_h is a
313 dependent variable during a microcracking sub-step but is updated directly during a
314 healing sub-step. In the latter, ζ_h is updated according to the new value of ω_h .

315 The vectors containing the values from all directions are denoted with bold non-italic
316 text. The values from a previous step, or sub-step, are denoted with the subscript p .

317 The integration over the hemispherical domain is evaluated numerically using
318 MacLaurin's 29 point integration rule (i.e. $n_d=29$) (Stroud 1973). These directions and the
319 associated integration weights are given in Appendix A. For convenience, Voigt notation
320 is used in the description of algorithm 1.

321

Algorithm 1. Computational algorithm

The starting variable values for all directions from the previous time step (null if first step) $\zeta_p, \zeta_{hp}, \mathbf{h}_{vp}$ & $\boldsymbol{\varepsilon}_{hp}$ and the total stress ($\boldsymbol{\sigma}$) to be updated for the new total strain $\boldsymbol{\varepsilon} + \Delta\boldsymbol{\varepsilon}$, for time t to $t+\Delta t$, noting that $\Delta t = \Delta t_n$	
Mechanical sub – step	
<i>for</i> $j = 1$ to n_d	Loop over spherical integration directions (see App. A for integration directions and weights)
$\boldsymbol{\varepsilon}_{L_j} = \mathbf{N}_{\varepsilon_j}(\boldsymbol{\varepsilon} + \Delta\boldsymbol{\varepsilon})$	Calculate local strain tensor
$\zeta_{ef}(\boldsymbol{\varepsilon}_{L_j})$ & $\zeta_{hef}(\boldsymbol{\varepsilon}_{L_j} - \boldsymbol{\varepsilon}_{hp_j})$	Find effective strains for original and healed material (eq. 5&12)
Update $\zeta_j(\zeta_{ef_j}, \zeta_{p_j}), \zeta_{h_j}(\zeta_{hef_j}, \zeta_{hp_j}), \omega_j(\zeta_j), \omega_{h_j}(\zeta_{h_j})$ $\Delta\omega_j = \omega_j - \omega_{p_j}$ & $\Delta\omega_{h_j} = \omega_{h_j} - \omega_{hp_j}$	Update local microcracking parameters and variables for original material (eq. 5-7) & healed material (eq. 11-12)
$h_{r_j} = h_{vp_j}(1 - \omega_{h_j})$	Compute the increments of the microcracking variables for original and healed material
$\mathbf{A}_j = [(1 - \omega_j)\mathbf{D}_L + h_{vp_j}(1 - \omega_{h_j})\mathbf{D}_{Lh}]$	Update the re-healing variable for microcracking
<i>end j loop</i>	Compute the local microcracking – healed constitutive tensor (see line below eq. 22)
$\zeta_{hp} = \zeta_h; \mathbf{h}_{vp} = \mathbf{h}_v; \mathbf{h}_{rp} = \mathbf{h}_r$	Close loop over integration directions
$\omega_{hp} = \omega_{hp}(\zeta_{hp})$	Record values of healing and re-microcracking variables that have been updated for new microcracking.
Healing sub-step, if healing is active	If healing is activated continue, else jump to end of section.
<i>for</i> $j = 1$ to n_d	Loop over spherical integration directions
$a_j = a_{p_j} + \Delta\omega_j$ $a_{r_j} = a_{rp_j} + \Delta h_{vp_j} \omega_{hp_j}$	Calculate proportions of material available for healing (eq. 23) and re-healing (eq. 27)
$h_{v_j} = h_{vp_j} e^{-\frac{\Delta t}{\tau}} + a_j(1 - e^{-\frac{\Delta t}{\tau}})$ $h_{r_j} = h_{rp_j} e^{-\frac{\Delta t}{\tau}} + \phi_{he} a_{r_j} (1 - e^{-\frac{\Delta t}{\tau}})$ $\Delta h_{v_j} = h_{v_j} - h_{vp_j}$ $\Delta h_{r_j} = h_{r_j} - h_{rp_j}$	Update the virgin healing and re-healing variables (eqs. 38 & 39) along with their increments (eqs. 29 & 30)
$\omega_{h_j} = 1 - \frac{(1 - \omega_{hp_j})^{h_{vp_j} + \Delta h_{v_j} + \Delta h_{r_j}}}{h_{v_j}}$	Update the healed material microcracking variables due to re-healing. (eq. 32)
Solve $\omega_{h_j} - \left(1 - \frac{\varepsilon_{h_j}}{\zeta_{h_j}} e^{-c \left(\frac{\zeta_{h_j} - \varepsilon_{h_j}}{\varepsilon_{h_0} - \varepsilon_{h_j}}\right)}\right) = 0$ for ζ_{h_j}	Update the nonlinear equation for the microcracking strain parameter for healing. (eq. 37)
$\boldsymbol{\varepsilon}_{h_j} = \frac{h_{v_j}(1 - \omega_{h_j})\boldsymbol{\varepsilon}_{L_j} - h_{v_j}(1 - \omega_{hp_j})(\boldsymbol{\varepsilon}_{L_j} - \boldsymbol{\varepsilon}_{hp_j})}{h_{v_j}(1 - \omega_{h_j})}$	Compute the current local healing strains (eq. 34)
$\mathbf{A}_j = [(1 - \omega_j)\mathbf{D}_L + h_{v_j}(1 - \omega_{h_j})\mathbf{D}_{Lh}]$	Update the local microcracking – healed constitutive tensor (eq. 22)
<i>end j loop</i>	Close loop over integration directions
End if: active healing	
$\mathbf{D}_{sech} = \left(\mathbf{I} + \frac{\mathbf{D}_{el}}{2\pi} \sum_{j=1}^{n_d} \mathbf{N}_{\varepsilon_j}^T [\mathbf{A}_j^{-1} - \mathbf{C}_L] \mathbf{N}_j w_{d_j} \right)^{-1} \mathbf{D}_{el}$	Update the secant stiffness (eq. 22)
$\boldsymbol{\varepsilon}_{Ch} = \mathbf{C} \boldsymbol{\alpha} \boldsymbol{\varepsilon}_h$	Update the total healing strain tensor, allowing for interactions (eq 35 and Appendix B), noting that the vector $\boldsymbol{\varepsilon}_h$ contains the stacked local healed strain vectors $\boldsymbol{\varepsilon}_{h_j}$ for all local directions $j=1$ to n_d
$\boldsymbol{\sigma} = \mathbf{D}_{sech}(\boldsymbol{\varepsilon} - \boldsymbol{\varepsilon}_{Ch})$	Compute the total stress.
end	

323

324

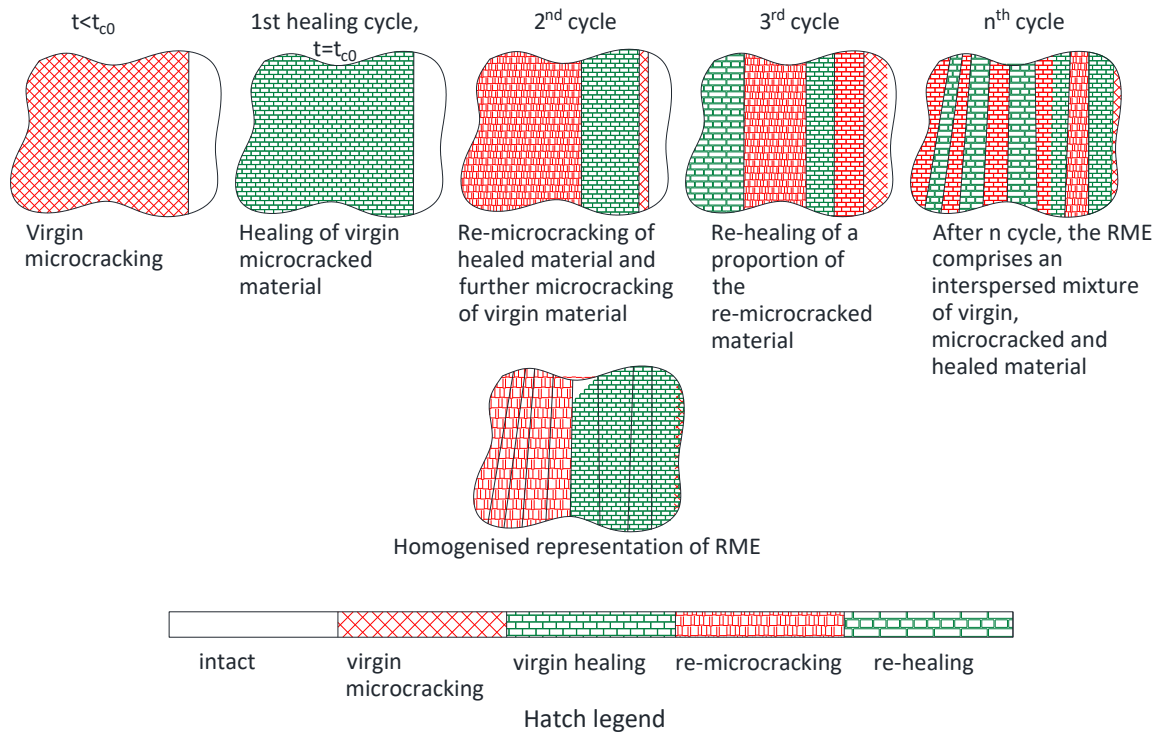
The schematics in Figure 3 illustrate the changing state of material during successive

325

microcracking-healing cycles within an RME, and the homogenised representation of the

326

RME based on equation 26.



327

328

Figure 3. Schematic representation of material states in successive microcracking and healing cycles

329

330

The new micromechanics based self-healing constitutive model was implemented in a

331

finite element code developed at Cardiff University. A standard virtual work formulation

332

was adopted to evaluate the stiffness matrix. Material nonlinearity was considered, and

333

the domain was assumed to be continuous throughout the loading history. The

334

nonlinear system of equations is solved using a standard Newton incremental iterative

335

scheme.

336 **3 Single point simulations**

337 A series of single-point simulations is presented in this section in order to illustrate the
338 performance of the proposed constitutive model. The material properties such as the
339 modulus of elasticity (E), tensile strengths (f_t) and Poisson's ratio for original and healed
340 materials (denoted by subscript h) that used for the simulations are given in Table 2. The
341 first example replicates a uniaxial tensile test with an applied strain rate of 5×10^{-6} /s in
342 the xx-direction. The simulations were undertaken for a range of curing time parameters
343 (see τ range in Table 2) and healing scenarios. The latter comprise no-healing (Nh), single
344 healing (Sh) and multiple healing (Mh) scenarios. 'Multiple healing' means that the
345 mechanism within the model to simulate an unlimited number of simultaneous
346 microcracking and healing steps is active.

347 The overall responses for each scenario, along with the associated evolutions of the
348 microcracking variables, are given in Figure 4.

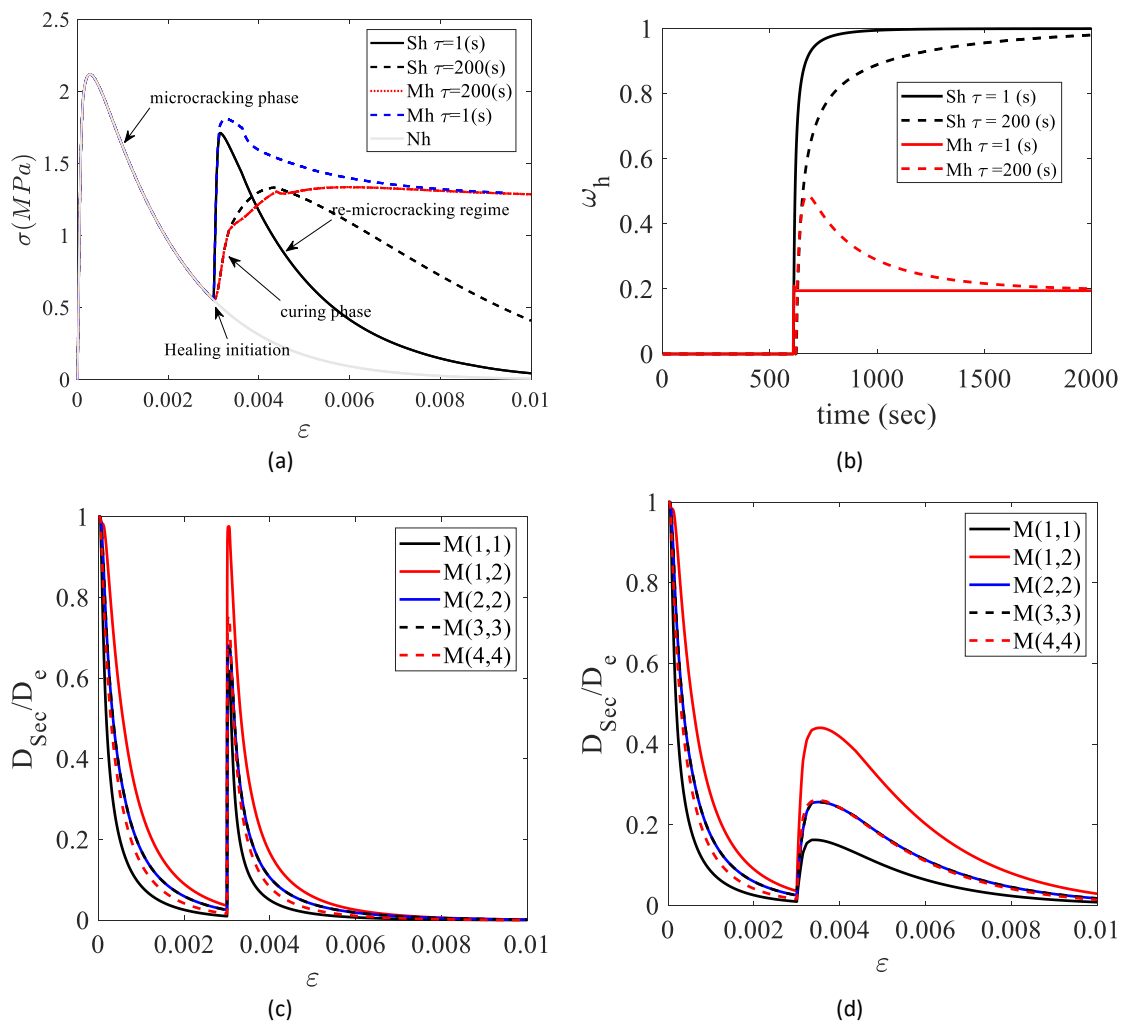
349 Table 2. Material properties

Variables	E (N/mm^2)	E_h (N/mm^2)	ν, ν_h	f_t, f_{th} (N/mm^2)	τ (s)	$\varepsilon_0, \varepsilon_{0h}$
Properties	24000	12000	0.15	1	1-60-200	0.0067

350 In this example, healing was assumed to commence when the strain reached 0.003.
351 For the material properties given, this strain value would be associated with substantial
352 microcracking in a real self-healing material and is approximately 70 times greater than
353 the crack initiation strain. It is noted that the healing activation criterion varies
354 considerably with the type of healing system and with the properties of the host
355 material.

356 The results show that the response is strongly affected by the value of the curing time
357 parameter with the healing response being less abrupt for larger values of τ . It is

358 noteworthy that the responses of the three healed material simulations tend to the same
 359 asymptotic stress, which is associated with balanced healing and microcracking rates.
 360 Furthermore, the ability of the model to capture anisotropic behaviour is explored by
 361 considering the changes to the components of the stiffness tensor over the prescribed
 362 strain path. The secant stiffness tensor (in Voigt matrix form) is normalised with the
 363 elasticity tensor (matrix), such that $\mathbf{M} = \mathbf{D}^{-1} \mathbf{D}_{\text{sech}}$. The component numbers shown in
 364 Figure 4c and 4d are selected matrix terms in Voigt notation. The changes in these matrix
 365 terms are illustrated in Figure 4c and d for $\tau=1$ and 200 (s) respectively. The results show
 366 that the relative matrix terms change in an anisotropic manner as microcracking and
 367 healing progress.



368 Figure 4. Computed uniaxial responses, a) variation of stress with time, b) re-
369 microcracking variables, c) Stiffness matrix component for $\tau = 1s$ and d) stiffness
370 matrix component for $\tau = 200s$.

371 In order to provide more insight into the anisotropic behaviour of the model, the
372 variation of the microcracking and healing variables for four selected directions have
373 been plotted for all three healing scenarios for the $\tau = 60s$ case in Figure 5. The direction
374 numbers correspond with the spherical integration directions given in Appendix A.

375 As may be expected, the maximum microcracking occurs in direction 1 which coincides
376 with the loading direction. The microcracking variable in direction 1 (i.e. ω_1) has a value
377 of 0.99 at the time healing initiates; by contrast, the corresponding value of $\omega_{28} = 0.90$.
378 The ω values for the directions that do not correspond with the loading direction
379 illustrate the effect of the local shear strains, as well as the local normal strains, on the
380 degree of microcracking around the hemisphere. As may be expected, the progression of
381 the microcracking and healing responses for the non-coincident directions lag those of
382 direction 1, with the lag increasing as the angle between direction 1 and the normal to
383 the local direction under consideration increases. The microcracking and healing
384 variables are visualised in the polar plots shown in Figure 5. These polar plots are given
385 at times 10, 20, 75 and 175 seconds for the microcracking variables and 610, 700, 800
386 and 1800 seconds for the healing and re-microcracking variables.

387

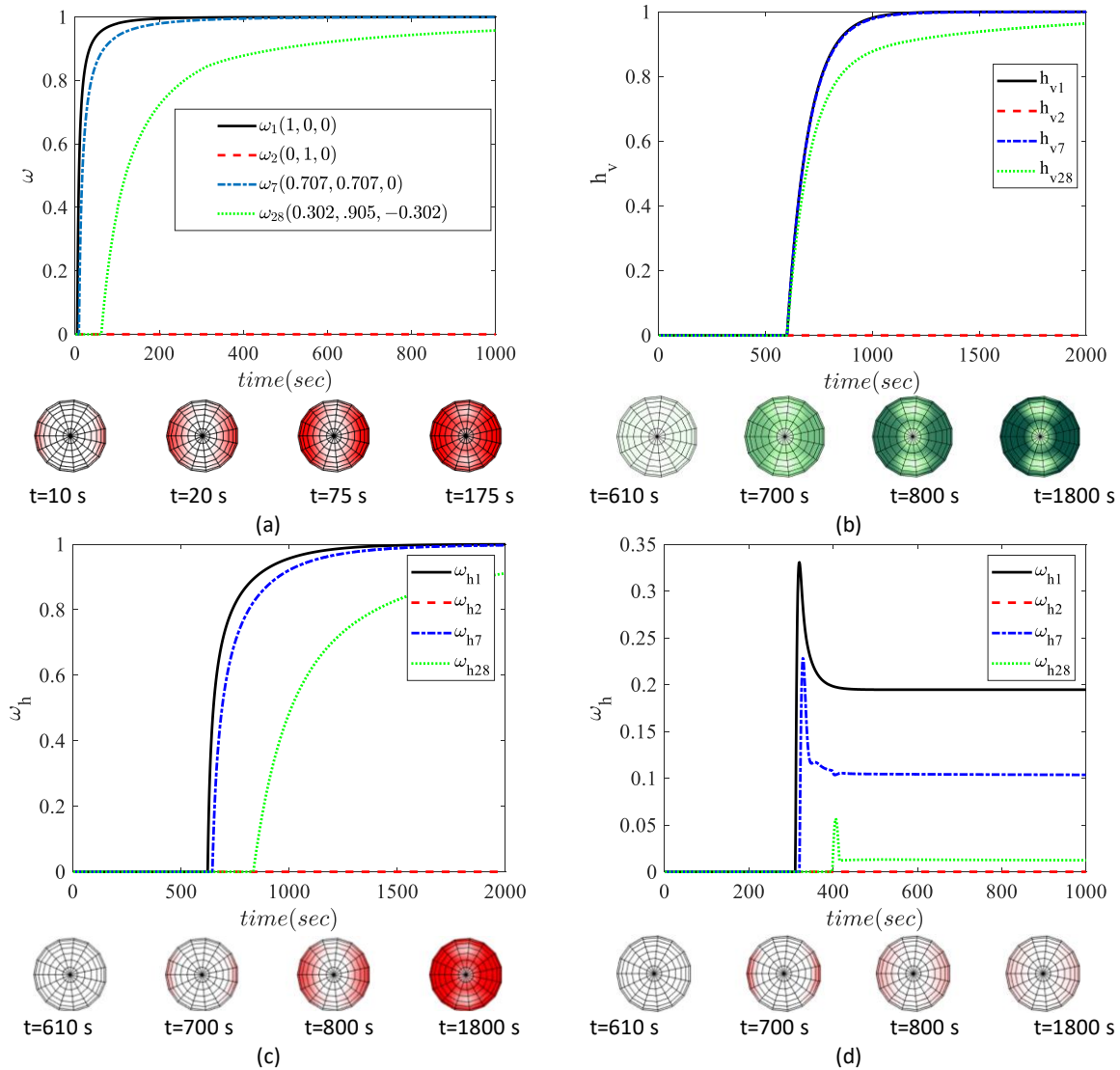
388

389

390

391

392



393 Figure 5. microcracking and healing variable evolution, a) virgin microcracking b) virgin
 394 healing, c) re-microcracking for single healing cycle and d) re-microcracking-re-healing
 395 variables for multiple healing cycles.

396 **3.1 Parametric study**

397 The results of a systematic parametric study are now presented in which the model was
 398 used to predict the uniaxial response of a self-healing cementitious sample. The
 399 reference properties are those given in Table 2. The material properties altered
 400 sequentially in the study were the curing time, healed material Young's modulus and

401 healed material strength. The sequence of values used for each parameter are given in

402 Table 3. The range of healing scenarios considered are as follows:

- 403 i) single healing under continuous monotonic loading ($\dot{\epsilon} = 5 \times 10^{-6} /s$):
- 404 ii) multiple microcracking-healing under continuous monotonic loading ($\dot{\epsilon} =$
- 405 $5 \times 10^{-6} /s$):
- 406 iii) multiple microcracking-healing events under loading-unloading-reloading
- 407 conditions (loading $\dot{\epsilon} = 5 \times 10^{-6}$; unloading $\dot{\epsilon} = -5 \times 10^{-6}$; reloading
- 408 rate varies as shown in Figure 6)

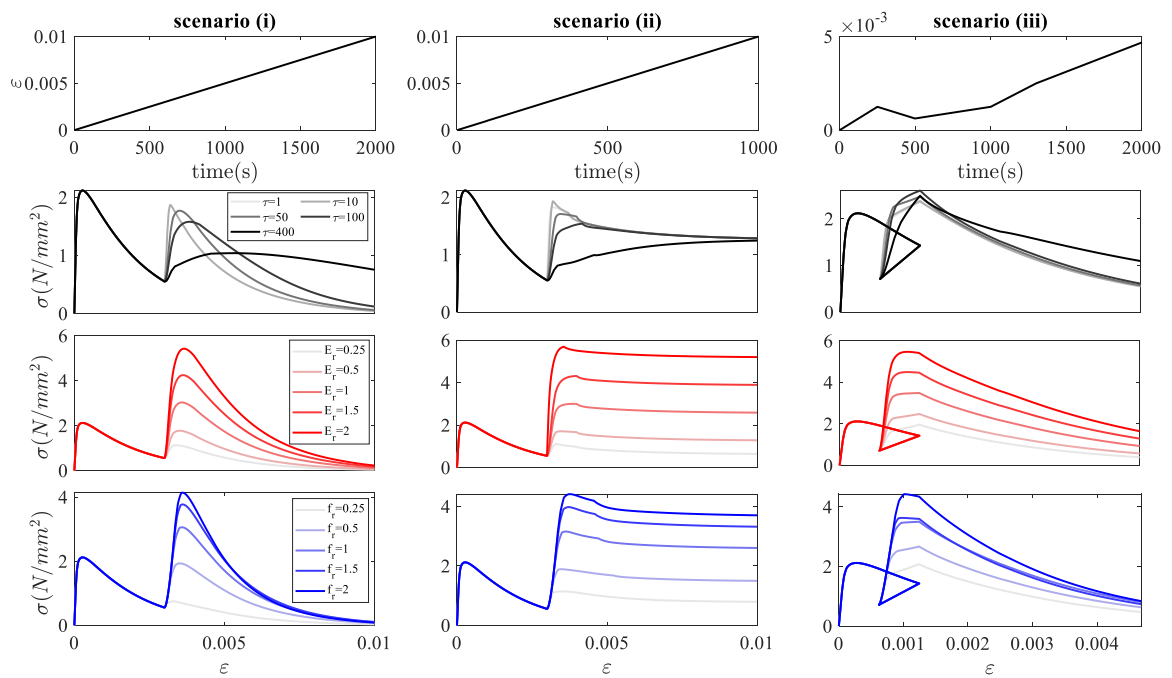
409 Table 3. material properties for parametric study

Case/material properties	Ranges	τ (sec)	E_h (N/mm ²)	f_{th} (N/mm ²)
τ	1, 10, 50, 100, 400	variable	12000	1
$E_r = E_h/E^*$	0.25, 0.5, 1, 1.5, 2	50	variable	1
$f_r f_{th}/f_t^{**}$	0.25, 0.5, 1, 1.5, 2	50	12000	variable

410 * E_r denotes the ratio of the elastic modulus of healing material to original material

411 ** f_r denotes the ratio of the tensile strength of healing material to original material

412



413

414 Figure 6. Parametric study results

415 Figure 6 presents the predicted mechanical response for all of the cases considered.
416 The relative effect of changing each parameter in turn is evident from the graphs, with
417 changes in the healed-material strength and stiffness greatly affecting the post-healed
418 peak load and post-peak softening response. As already mentioned, changing τ has a
419 profound influence on the apparent stiffness and ductility of the post-healed response,
420 with lower values of τ being associated with lower post-healed peak strengths and an
421 apparent more ductile response.

422 For real cases, the model parameters are calibrated by using experimental data from
423 uniaxial microcracking tests to determine the softening parameters of equation (7), such
424 that the peak and post-peak behaviour are captured accurately. Then, the healing-
425 efficiency parameter (ϕ_{he}) is found using data from uniaxial microcracking – healing tests,
426 with ϕ_{he} being calibrated such that the computed overall stiffness recovery matches the
427 corresponding experimental value. The healing activation time is obtained through
428 direct observation. These microcracking and healing parameters are variable since they
429 depend on the mechanical properties of the overall self-healing system, as well as those
430 of the components, such as microcapsule shells and vascular network channels.

431 **3.2 Microencapsulated uniaxial test**

432 The proposed model's ability to replicate the mechanical response of samples formed
433 from a self-healing cementitious material containing microcapsules is assessed by
434 considering the experimental tests on a set of cylindrical samples undertaken by James
435 et al. (2014). In this work, the investigators measured the effects of healing on the elastic
436 modulus of a microencapsulated self-healing cementitious material system. The tests
437 considered material samples formed with 400-500 μm sized micro-capsules containing

438 sodium silicate at dosages of 0.5% and 1% by volume of the cement paste. The tests
439 followed a procedure from ASTM C469 for measuring the static elastic modulus. Each
440 cylindrical sample was loaded axially up to 70% of the nominal compressive strength in
441 order to induce a degree of microcracking. The samples were then unloaded and allowed
442 to heal for 3 days and then reloaded to failure.

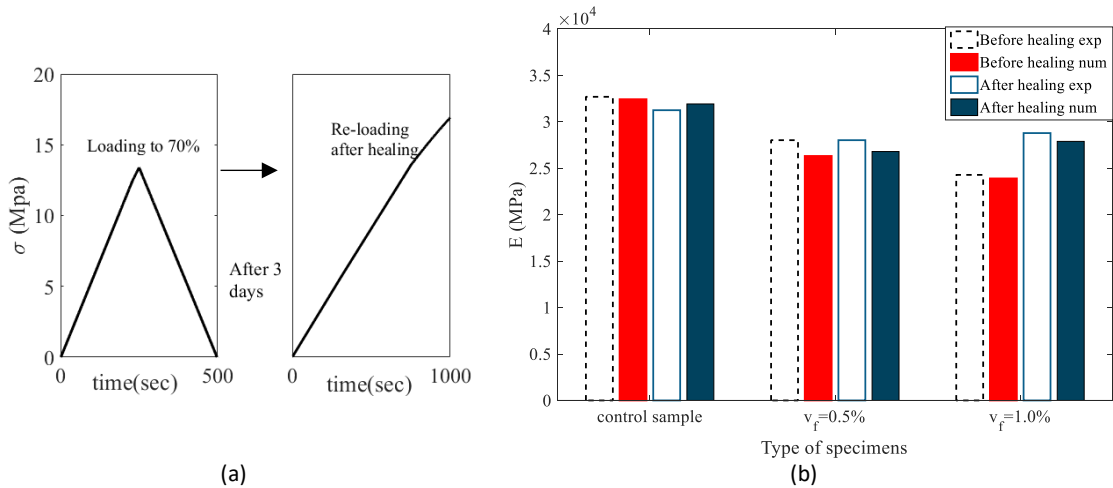
443 The material properties used for the simulations are presented in Table 4.

444 Table 4. Material properties

Material/properties	E (N/mm ²)	ν	f_t (N/mm ²)	445
Matrix	32430	0.25	1	0.0025
Capsule	3000	0.2	-	
Healing agent	3000	0.2	5	0.0003

447 The results of the simulations are presented in Figure 7, with Figure 7a giving the
448 loading protocol and Figure 7b the experimental and numerical values of the elastic
449 moduli before and after healing for each case. It is evident from the differences between
450 the initial stiffnesses of the control samples and the samples containing microcapsules
451 that the presence of the microcapsules reduced the stiffness of the material.

452 The results of the samples with microcapsules shows that the model is able to
453 reproduce the increase in stiffness brought about by healing, and to capture the effect
454 of increasing the dosage of microcapsules. It is noted that the experimental data did not
455 include any load-displacement responses.



456 Figure 7. Experimental validation, a) loading protocol, b) stiffness recovery
 457 comparison

458 **4 Finite element example: self-healing beam tests.**

459 The 3-point beam bending experiments conducted by Ferrara *et al.* (2014) are
 460 considered in this example. In these experiments, concrete beams of size 450×100×50
 461 mm (Figure 8a), were cast and loaded until the crack mouth opening displacement
 462 (CMOD) reached 150 μ m and 300 μ m for first and second healing cycle respectively. Some
 463 of these beams were formed from a standard concrete mix and others were formed with
 464 a concrete containing a proprietary crystalline admixture (CA) (Ferrara *et al.* 2014), which
 465 was assumed to act as an autogenous healing enhancer. After cracking, each sample was
 466 stored for 12 months in either, (i) dry air or (ii) a water curing tank. The beams were then
 467 re-loaded until failure. The cases considered are summarised in Table 5.

468 The material properties used for the simulations (see Table 5) were based on those
 469 reported by Di Luzio *et al.* (2018); Ferrara *et al.* (2014) and Cibelli *et al.* (2022). The beam
 470 was modelled with the finite element program containing the new constitutive model.
 471 The testing arrangement, specimen geometry, boundary conditions and finite element
 472 mesh used for the analysis are illustrated in Figure 8.

473

Table 5 material properties used for BVP simulation.

Case/ parameter	Curing condition	Name	E, E_h (N/mm^2)	ν, ν_h	f_t (N/mm^2)	f_{th} (N/mm^2)	τ (days)	ϕ_{he}	$\epsilon_0, \epsilon_{0h}$
Healing without CA	Dry	WCAD	35000	0.25	0.1	0.5	270	0.01	0.0025
Healing without CA	Wet	WCAW	35000	0.25	0.3	0.5	270	0.02	0.0025
Healing with CA	Dry	CAD	35000	0.25	0.45	0.5	135	0.08	0.0025
Healing with CA	wet	CAW	35000	0.25	0.5	0.5	135	0.1	0.0025

474

The simulations of the control specimens (without CA) only considered the first healing

475

cycle, since no appreciable healing was observed in the second cycle. By contrast, the

476

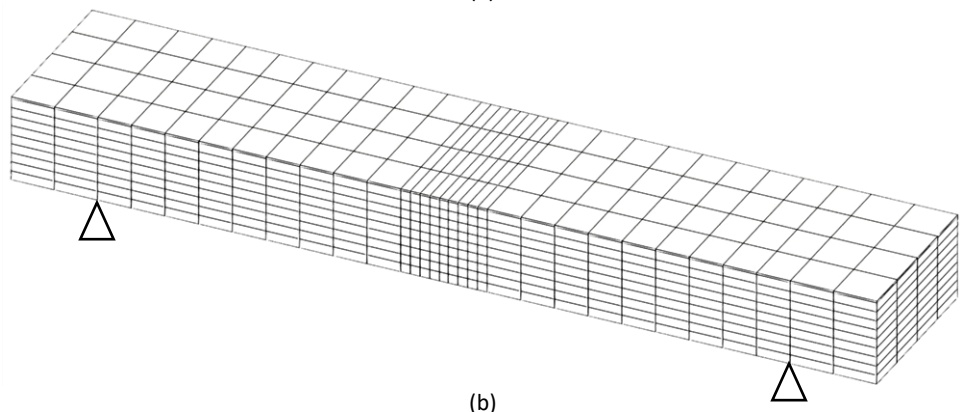
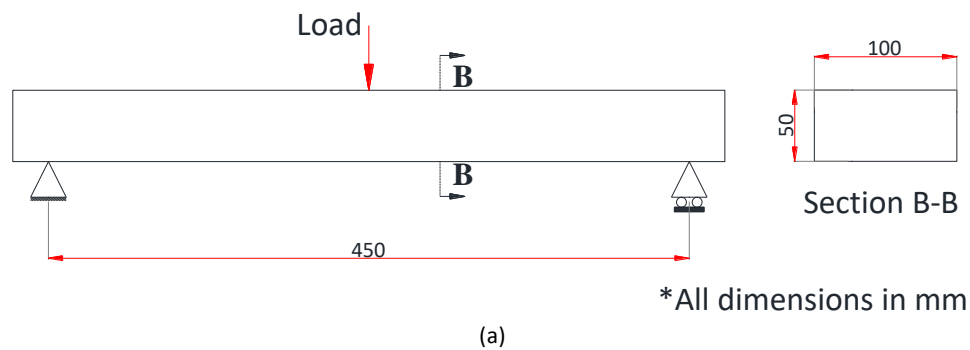
second healing cycle was considered for the specimens with CA. This is because

477

negligible healing was observed in the first cycle for the CA samples, but significant

478

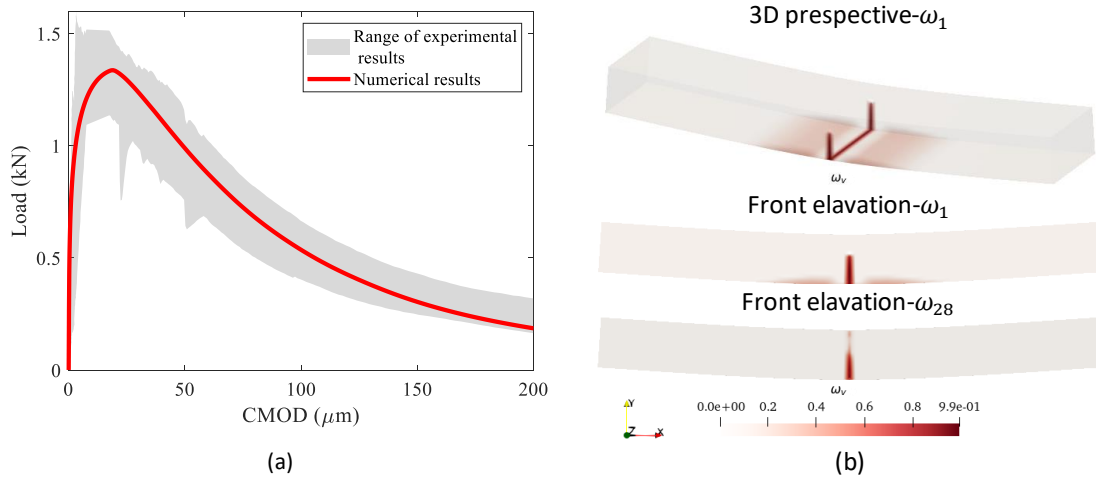
healing was measured for the second cycle.



479

Figure 8. (a) Beam geometry and boundary conditions, b) finite element mesh

480 The experimental and numerical responses of the control samples are given in Figure
 481 9, which also shows the distribution of selected microcracking variables. The results
 482 show that the model is able to simulate the overall response of the control specimens
 483 with good accuracy.

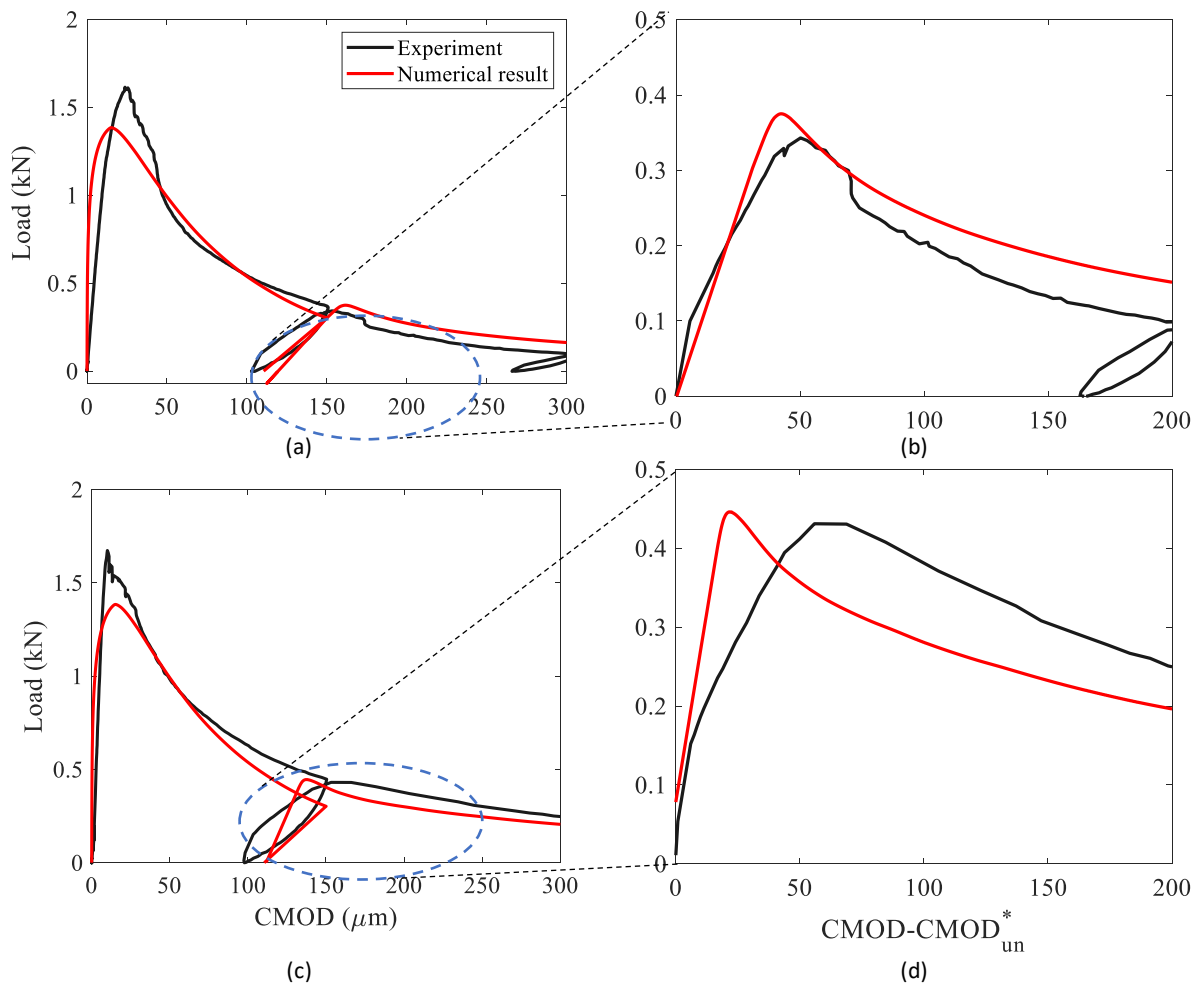


484 Figure 9. Experimental and numerical control beam responses, a) load v CMOD
 485 response, b) microcracking variables at a CMOD of 150 μm

486 The mean experimental and numerical load-CMOD responses, for the samples without
 487 and with CA, are given in Figure 10 and Figure 11 respectively. In these graphs, the post-
 488 curing reloading response commences from the unloading point of the initial cracking
 489 stage.

490

491



492

493 Figure 10 Load-CMOD response for WCAD samples (a-b) and WCAW (c-d), a) loading -

494 reloading response with healing, b) magnified illustration of (a), c) reloading with

495 healing for WCAW, and d) magnified illustration of (c)

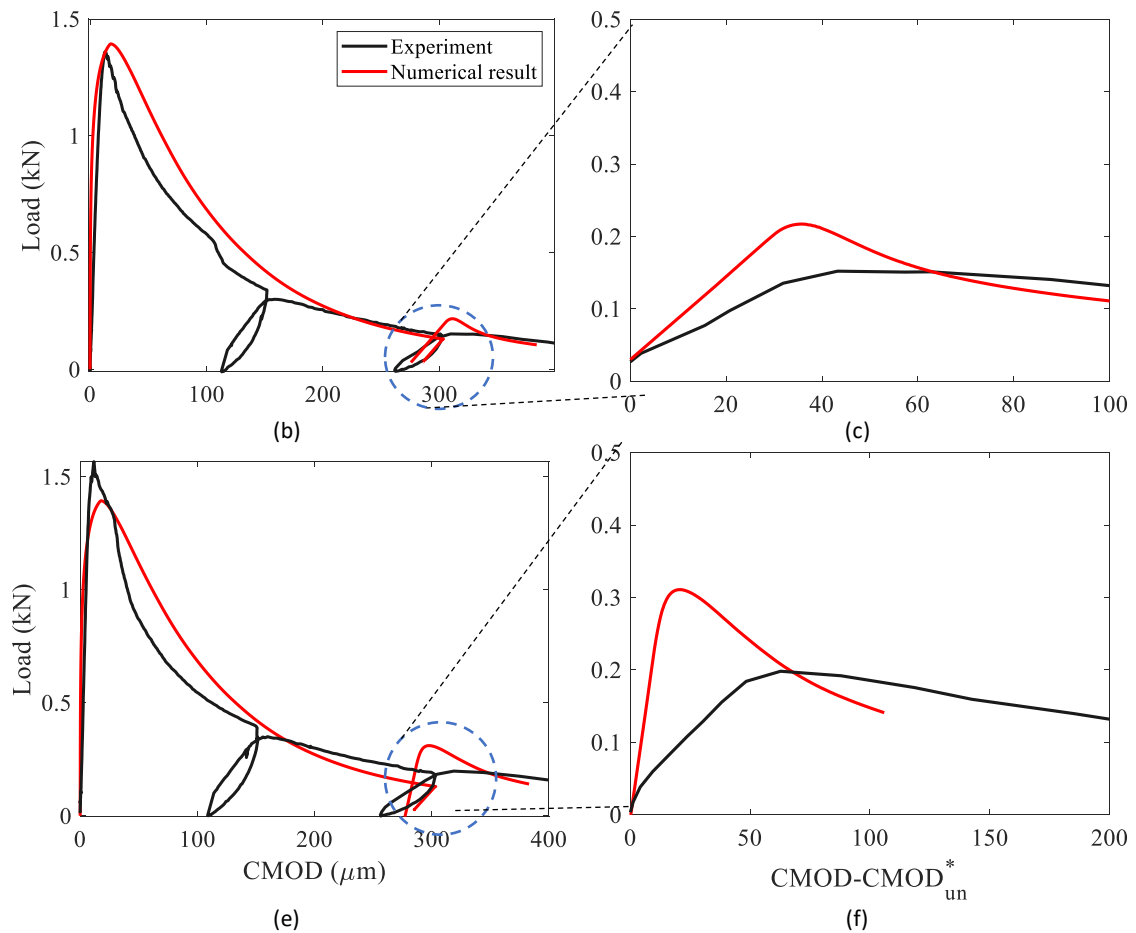
496

497

498

499

500



501 Figure 11. Load-CMOD response for samples with CA cured in dry (CAD) (a-b) and wet
 502 conditions (c-d) (CAW), a) loading reloading process with healing for CAD, b) magnified
 503 illustration of (a), c) Loading reloading with healing for CAW and d) magnified
 504 illustration of (c)

505 Comparing Figure 10b and c with 10e and f, shows that the stiffness and strength
 506 recoveries due to healing were significantly less for dry cured specimens than for the
 507 wet-cured specimens without CA. The model captures this difference, although does
 508 show a small increase in post-healed strength for the dry specimens that was not evident
 509 in the corresponding 'wet' experiments. However, in wet conditions the strengths
 510 increased up to 10%. The effect of CA on mechanical recovery shows itself in both
 511 strength and stiffness regains, as illustrated in Figure 11 c and f.

512 Figure 12 gives plots that show the distribution of the healing and re-microcracking
 513 variables at selected stages of the analysis for the CAW case. Figure 12a shows that, at

514 the start of reloading stage, the healed material re-microcracking value is zero, since at
515 this point the healed material has just formed in a stress-free condition. It subsequently
516 experiences microcracking. Re-microcracking values for the normal crack direction are
517 shown in Figure 12 b and c for CMOD values of 310 and 350 μm respectively. This figure
518 also shows that the further microcracking is localised where healing material was
519 formed.

520

521

522

523

524

525

526

527

528

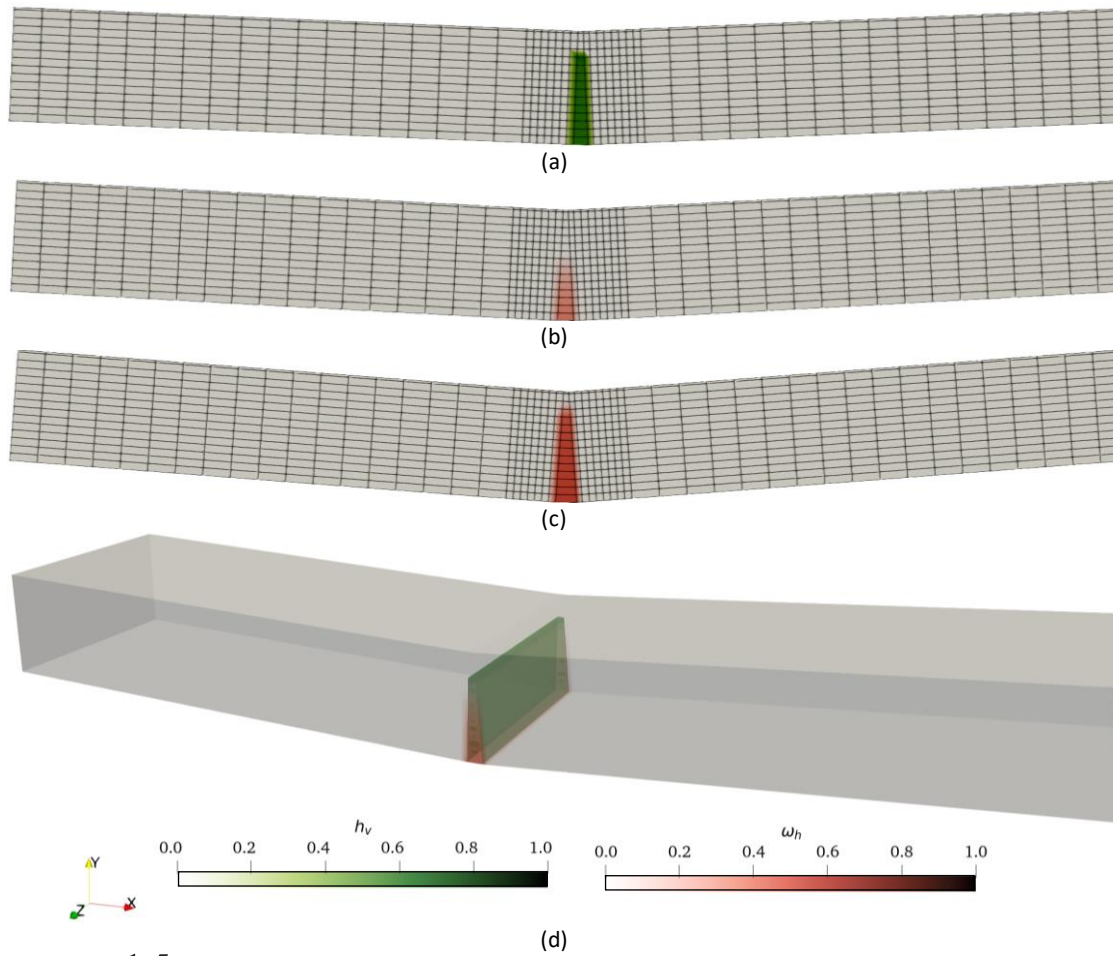
529

530

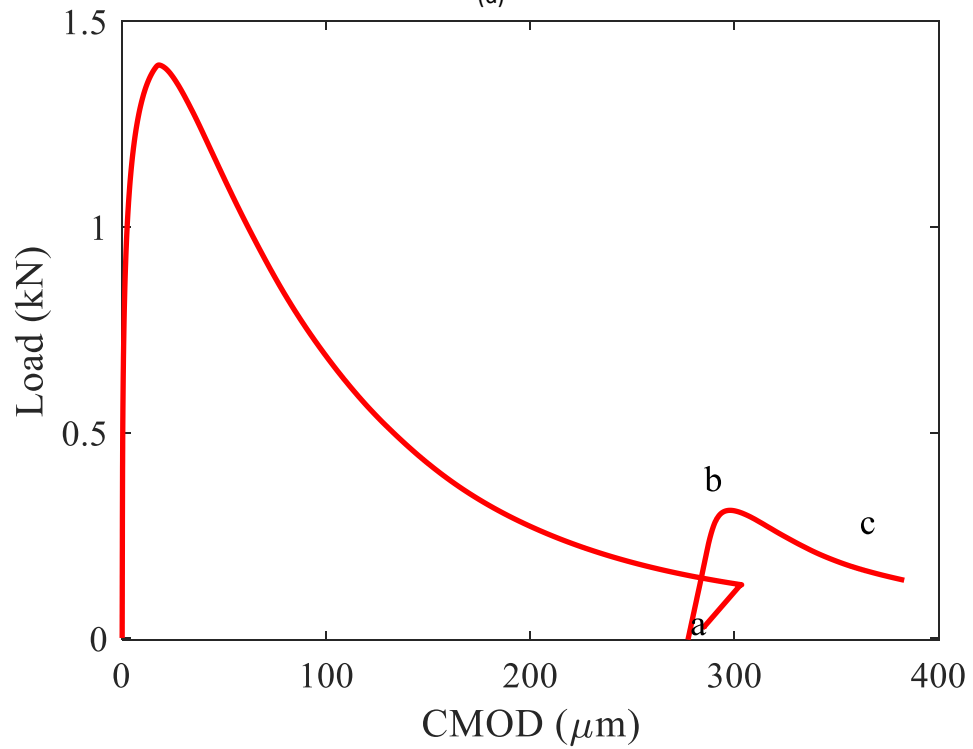
531

532

533



(d)



(e)

534 Figure 12. Healed material status after reloading a) healing at $CMOD = 275 \mu m$, b) re-
 535 microcracked at $CMOD = 310 \mu m$ c) re-cracking at $CMOD = 350 \mu m$, d) overlapping
 536 cracking and healing illustration, and e) load-CMOD response for CAW

537

538 **5 Conclusions**

539 A new micromechanical model for simulating the response of self-healing cementitious
540 materials has been presented in this paper. The proposed constitutive formulation
541 captures the time-dependent behaviour of these materials with good accuracy using
542 relatively few physically meaningful material parameters.

543 The model simulates microcracking and its healing using the assumption that all
544 microcracked material has the potential to be healed. The micromechanical formulation
545 is well suited to simulating distributed cracking and healing for systems in which the
546 healing material is spread throughout the structural element. This applies to healing
547 systems that use embedded microcapsules. The model is not aimed at simulating
548 discrete cracks or systems that use vascular networks, although some aspects of the
549 behaviour of the latter can be captured by the model.

550 The constitutive model was implemented in a 3D finite element framework for
551 simulating boundary value problems. Based on the results, the following conclusions can
552 be drawn:

- 553 • the mechanical properties of healed material -often a healing-agent cementitious-
554 matrix composite- greatly affect the post-cracking mechanical response of self-
555 healing materials:
- 556 • the recursive scheme used to update the healing and re-cracking variables is an
557 effective way to simulate the response of elements to multiple and continuous
558 microcracking-healing cycles in a computationally efficient manner:

- 559
- the model predictions exhibit significant anisotropy due to the directional variations in the degrees of microcracking and healing.
- 560
- a series of simulations, including a parametric study, shows that the overall microcracking-healing response is strongly dependent on the curing time parameter of the self-healing agent, as well as the degree of microcracking at which healing is assumed to commence:
- 561
- 562
- 563
- 564
- the proposed model can simulate different types of self-healing scenarios and is able to replicate the behaviour of structural elements undergoing simultaneous microcracking and healing.
- 565
- 566
- 567

568

569 **Acknowledgement**



572

This project has received funding from the European Union's Horizon 2020 research and innovation programme under the Marie Skłodowska-Curie grant agreement No 860006. We acknowledge the support of the Supercomputing Wales project, which is part-funded by the European Regional Development Fund (ERDF) via Welsh Government.

573

574

575

576

577

578

579

580

581

582

583

584

585

586

587

588

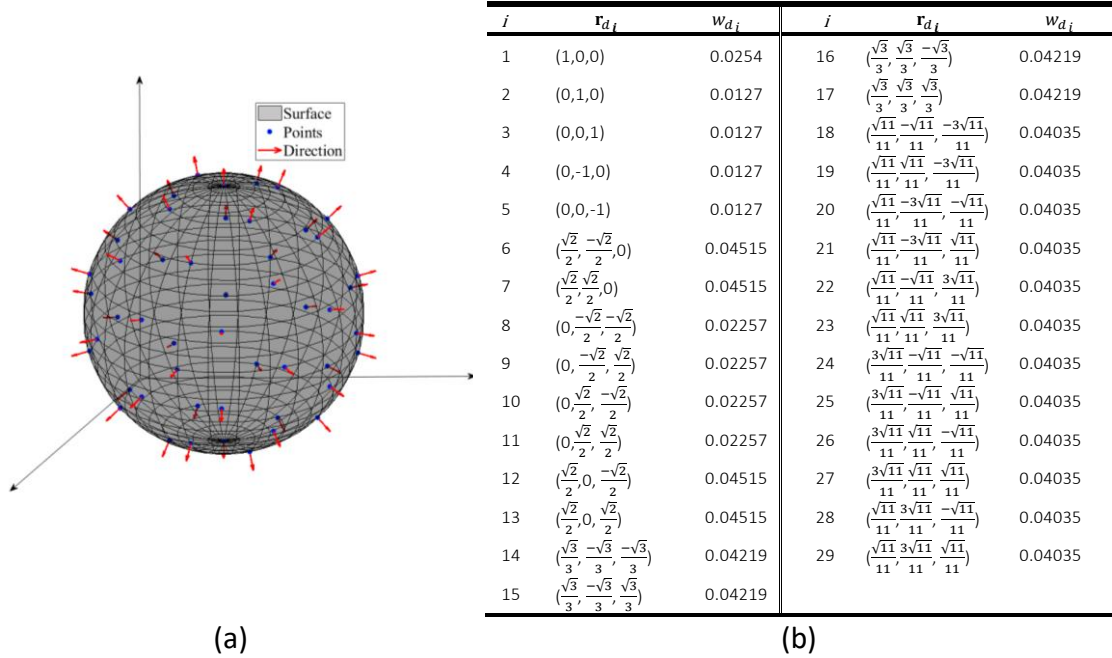
589

590

591

592 **Appendix A. Weights and corresponding directions for spherical numerical**
 593 **integration**

594 Point number i , direction \mathbf{r}_{d_i} (also equals the position on a unit hemisphere) and
 595 integration weights w_{d_i} .



596 Figure A.1 Spherical integration directions, a) positions on a sphere, b) numerical
 597 integration directions and weights

598
 599

600 **Appendix B. Thermodynamic consistency**

601 The constitutive formulation should be consistent with the second law of
 602 thermodynamics. This may be satisfied, during healing, if the model ensures that no
 603 energy is created due to healing alone. The condition implies that the stress tensor in
 604 local and global coordinates before and after an increment of healing should be the
 605 same; thus, the corresponding eigenstrain for each healed set of microcracks is
 606 evaluated such that the overall global stress does not change due to healing alone. This
 607 condition may be expressed mathematically as follows, noting that here i and $i-1$ refer
 608 to states before and after a healing sub-step respectively:

$$\boldsymbol{\sigma}_i = \mathbf{D}_{\text{sech}} \cdot (\boldsymbol{\varepsilon} - \boldsymbol{\varepsilon}_{\text{ah}}) = \boldsymbol{\sigma}_{i-1} \quad (\text{B.1})$$

609 Re-arranging the above equation gives:

$$\boldsymbol{\varepsilon}_{\text{ah}} = \boldsymbol{\varepsilon} - \mathbf{D}_{\text{sech}}^{-1} \boldsymbol{\sigma}_{i-1} \quad (\text{B.2})$$

610 $\boldsymbol{\varepsilon}_{\text{ah}}$ is given in equation (18). To allow for interaction effects between microcracking
611 directions, a variable α has been added to the equation. The resulting equations in
612 standard and discretised forms are given B.3 and B.4 respectively.

$$\boldsymbol{\varepsilon}_{\text{Gh}} = \frac{1}{2\pi} \oint\!\!\!\oint_s \mathbf{N}_\varepsilon \cdot \left[\frac{(1-\omega)}{h_v(1-\omega_h)} \mathbf{C}_{\text{Lh}} \cdot \mathbf{D}_L + \mathbf{I}^{2s} \right]^{-1} : \boldsymbol{\alpha} : \boldsymbol{\varepsilon}_h \quad (\text{B.3})$$

$$\boldsymbol{\varepsilon}_{\text{Gh}} = \sum_{id=1}^{29} \mathbf{N}_{\varepsilon_{id}} \cdot \left[\frac{(1-\omega_{id})}{h_{v_{id}}(1-\omega_{h_{id}})} \mathbf{C}_{\text{Lh}} \cdot \mathbf{D}_L + \mathbf{I}^{2s} \right]^{-1} \alpha_{id} \boldsymbol{\varepsilon}_{h_{id}} \quad (\text{B.4})$$

613

614 The aim is to find α_{id} such that equation B.1 is satisfied, with $\boldsymbol{\varepsilon}_{\text{Gh}}$ in place of $\boldsymbol{\varepsilon}_{\text{ah}}$;
615 however, this gives 6 equations with 87 unknowns as noted below. This equation is
616 therefore an undetermined equation which has an infinite number of solutions. This may
617 be resolved by applying the least squares constraint and assuming that $\mathbf{N}_{\varepsilon_{id}} \cdot \mathbf{N}_{\varepsilon_{id}} \cdot$

618 $\left[\frac{(1-\omega_{id})}{h_{v_{id}}(1-\omega_{h_{id}})} \mathbf{C}_{\text{Lh}} \cdot \mathbf{D}_L + \mathbf{I}^{2s} \right]^{-1}$ is a coefficient matrix for each direction considered (i.e. each

619 spherical integration direction), as follows:

$$\sum_{id=1}^{29} \begin{bmatrix} C_{11}^{id} & C_{12}^{id} & C_{13}^{id} \\ C_{21}^{id} & C_{22}^{id} & C_{23}^{id} \\ C_{31}^{id} & C_{32}^{id} & C_{33}^{id} \\ C_{41}^{id} & C_{42}^{id} & C_{43}^{id} \\ C_{51}^{id} & C_{52}^{id} & C_{53}^{id} \\ C_{61}^{id} & C_{62}^{id} & C_{63}^{id} \end{bmatrix} \begin{bmatrix} \varepsilon_{h_1}^{id} \\ \varepsilon_{h_2}^{id} \\ \varepsilon_{h_3}^{id} \end{bmatrix} \alpha_{id} = \begin{bmatrix} \varepsilon_{\text{Gh}_1} \\ \varepsilon_{\text{Gh}_2} \\ \varepsilon_{\text{Gh}_3} \\ \varepsilon_{\text{Gh}_4} \\ \varepsilon_{\text{Gh}_5} \\ \varepsilon_{\text{Gh}_6} \end{bmatrix} \quad (\text{B.5})$$

620 Expanding the above series leads to following 6 equations:

$$\begin{bmatrix} C_{11}^1 \varepsilon_{h_1}^1 + C_{12}^1 \varepsilon_{h_2}^1 + C_{13}^1 \varepsilon_{h_3}^1 + C_{11}^2 \varepsilon_{h_1}^2 + C_{12}^2 \varepsilon_{h_2}^2 + C_{13}^2 \varepsilon_{h_3}^2 & \cdots & C_{11}^{29} \varepsilon_{h_1}^{29} + C_{12}^{29} \varepsilon_{h_2}^{29} + C_{13}^{29} \varepsilon_{h_3}^{29} \\ C_{21}^1 \varepsilon_{h_1}^1 + C_{22}^1 \varepsilon_{h_2}^1 + C_{23}^1 \varepsilon_{h_3}^1 + C_{21}^2 \varepsilon_{h_1}^2 + C_{22}^2 \varepsilon_{h_2}^2 + C_{23}^2 \varepsilon_{h_3}^2 & \cdots & C_{21}^{29} \varepsilon_{h_1}^{29} + C_{22}^{29} \varepsilon_{h_2}^{29} + C_{23}^{29} \varepsilon_{h_3}^{29} \\ C_{31}^1 \varepsilon_{h_1}^1 + C_{32}^1 \varepsilon_{h_2}^1 + C_{33}^1 \varepsilon_{h_3}^1 + C_{31}^2 \varepsilon_{h_1}^2 + C_{32}^2 \varepsilon_{h_2}^2 + C_{33}^2 \varepsilon_{h_3}^2 & \cdots & C_{31}^{29} \varepsilon_{h_1}^{29} + C_{32}^{29} \varepsilon_{h_2}^{29} + C_{33}^{29} \varepsilon_{h_3}^{29} \\ C_{41}^1 \varepsilon_{h_1}^1 + C_{42}^1 \varepsilon_{h_2}^1 + C_{43}^1 \varepsilon_{h_3}^1 + C_{41}^2 \varepsilon_{h_1}^2 + C_{42}^2 \varepsilon_{h_2}^2 + C_{43}^2 \varepsilon_{h_3}^2 & \cdots & C_{41}^{29} \varepsilon_{h_1}^{29} + C_{42}^{29} \varepsilon_{h_2}^{29} + C_{43}^{29} \varepsilon_{h_3}^{29} \\ C_{51}^1 \varepsilon_{h_1}^1 + C_{52}^1 \varepsilon_{h_2}^1 + C_{53}^1 \varepsilon_{h_3}^1 + C_{51}^2 \varepsilon_{h_1}^2 + C_{52}^2 \varepsilon_{h_2}^2 + C_{53}^2 \varepsilon_{h_3}^2 & \cdots & C_{51}^{29} \varepsilon_{h_1}^{29} + C_{52}^{29} \varepsilon_{h_2}^{29} + C_{53}^{29} \varepsilon_{h_3}^{29} \\ C_{61}^1 \varepsilon_{h_1}^1 + C_{62}^1 \varepsilon_{h_2}^1 + C_{63}^1 \varepsilon_{h_3}^1 + C_{61}^2 \varepsilon_{h_1}^2 + C_{62}^2 \varepsilon_{h_2}^2 + C_{63}^2 \varepsilon_{h_3}^2 & \cdots & C_{61}^{29} \varepsilon_{h_1}^{29} + C_{62}^{29} \varepsilon_{h_2}^{29} + C_{63}^{29} \varepsilon_{h_3}^{29} \end{bmatrix} = \begin{bmatrix} \varepsilon_{Gh_1} \\ \varepsilon_{Gh_2} \\ \varepsilon_{Gh_3} \\ \varepsilon_{Gh_4} \\ \varepsilon_{Gh_5} \\ \varepsilon_{Gh_6} \end{bmatrix} \quad (B.6)$$

621

$$\begin{bmatrix} C_{11}^1 & C_{12}^1 & C_{13}^1 & C_{11}^2 & C_{12}^2 & C_{13}^2 & \cdots & C_{11}^{29} & C_{12}^{29} & C_{13}^{29} \\ C_{21}^1 & C_{22}^1 & C_{23}^1 & C_{21}^2 & C_{22}^2 & C_{23}^2 & \cdots & C_{21}^{29} & C_{22}^{29} & C_{23}^{29} \\ C_{31}^1 & C_{32}^1 & C_{33}^1 & C_{31}^2 & C_{32}^2 & C_{33}^2 & \cdots & C_{31}^{29} & C_{32}^{29} & C_{33}^{29} \\ C_{41}^1 & C_{42}^1 & C_{43}^1 & C_{41}^2 & C_{42}^2 & C_{43}^2 & \cdots & C_{41}^{29} & C_{42}^{29} & C_{43}^{29} \\ C_{51}^1 & C_{52}^1 & C_{53}^1 & C_{51}^2 & C_{52}^2 & C_{53}^2 & \cdots & C_{51}^{29} & C_{52}^{29} & C_{53}^{29} \\ C_{61}^1 & C_{62}^1 & C_{63}^1 & C_{61}^2 & C_{62}^2 & C_{63}^2 & \cdots & C_{61}^{29} & C_{62}^{29} & C_{63}^{29} \end{bmatrix}_{6 \times 87} \begin{bmatrix} \alpha_1 \varepsilon_{h_1}^1 \\ \alpha_1 \varepsilon_{h_2}^1 \\ \alpha_1 \varepsilon_{h_3}^1 \\ \alpha_2 \varepsilon_{h_1}^2 \\ \alpha_2 \varepsilon_{h_2}^2 \\ \alpha_2 \varepsilon_{h_3}^2 \\ \vdots \\ \alpha_{29} \varepsilon_{h_1}^{29} \\ \alpha_{29} \varepsilon_{h_2}^{29} \\ \alpha_{29} \varepsilon_{h_3}^{29} \end{bmatrix}_{87 \times 1} = \begin{bmatrix} \varepsilon_{Gh_1} \\ \varepsilon_{Gh_2} \\ \varepsilon_{Gh_3} \\ \varepsilon_{Gh_4} \\ \varepsilon_{Gh_5} \\ \varepsilon_{Gh_6} \end{bmatrix}_{6 \times 1} \quad (B.7)$$

622

623 This is rewritten in matrix form as:

$$624 \quad \boldsymbol{\varepsilon}_{Gh} = \mathbf{C} \boldsymbol{\alpha} \boldsymbol{\varepsilon}_h \quad (B.8)$$

625 Equation (B.8) is solved for the unknowns $\boldsymbol{\alpha}$, with $\boldsymbol{\varepsilon}_{Gh}$ in the right-hand-side being

626 equal to $\boldsymbol{\varepsilon}_{ah}$ from equation (B.2).

627 6 References

628 Abu Al-Rub, R. K., & Darabi, M. K. (2012). A thermodynamic framework for constitutive
629 modeling of time- and rate-dependent materials. Part I: Theory. *International Journal*
630 *of Plasticity*, **34**. doi:10.1016/j.ijplas.2012.01.002

631 Arnold, J. S., & Adam, J. A. (1999). A simplified model of wound healing II: The critical
632 size defect in two dimensions. *Mathematical and Computer Modelling*, **30**(11–12).
633 doi:10.1016/S0895-7177(99)00197-1

634 Barbero, E. J., Greco, F., & Lonetti, P. (2005). Continuum Damage-Healing Mechanics
635 with application to self-healing composites. *International Journal of Damage*
636 *Mechanics*, **14**(1), 51–81.

637 Budiansky, B., & O’connell, R. J. (1976). Elastic moduli of a cracked solid. *International*
638 *Journal of Solids and Structures*, **12**(2), 81–97.

639 Chen, Q., Li, W., & Jiang, Z. (2022). Theoretical estimation of the elastic moduli of self-
640 healing concrete relevant to the evolution of cracks closing due to crystallization- and
641 precipitation-based mechanism. *Journal of Building Engineering*, **58**.
642 doi:10.1016/j.jobe.2022.104995

643 Cibelli, A., Pathirage, M., Cusatis, G., Ferrara, L., & Di Luzio, G. (2022). A discrete
644 numerical model for the effects of crack healing on the behaviour of ordinary plain
645 concrete: Implementation, calibration, and validation. *Engineering Fracture Mechanics*,
646 **263**, 108266.

647 Darabi, M. K., Abu Al-Rub, R. K., & Little, D. N. (2012). A continuum damage mechanics
648 framework for modeling micro-damage healing. *International Journal of Solids and*
649 *Structures*, **49**(3–4). doi:10.1016/j.ijsolstr.2011.10.017

650 Davies, R., & Jefferson, A. (2017). Micromechanical modelling of self-healing
651 cementitious materials. *International Journal of Solids and Structures*, **113–114**, 180–
652 191.

653 Di Luzio, G., Ferrara, L., & Krelani, V. (2018). Numerical modeling of mechanical regain
654 due to self-healing in cement based composites. *Cement and Concrete Composites*, **86**.
655 doi:10.1016/j.cemconcomp.2017.11.006

656 Dutta, S., & Kishen, J. M. C. (2019). Micromechanical Damage Model for Plain Concrete
657 Considering Propagation of Matrix Microcracks. *Physical Mesomechanics*, **22**(2), 96–
658 106.

659 Ferrara, L., Krelani, V., & Carsana, M. (2014). A “fracture testing” based approach to
660 assess crack healing of concrete with and without crystalline admixtures. *Construction
661 and Building Materials*, **68**. doi:10.1016/j.conbuildmat.2014.07.008

662 Freeman, B. L., & Jefferson, A. (2023). A 3D Coupled Finite-Element Model for
663 Simulating Mechanical Regain in Self-Healing Cementitious Materials. *Journal of
664 Engineering Mechanics*, **149**(7), 04023038.

665 Freeman, B. L., & Jefferson, A. D. (2022). A 3D coupled chemo-mechanical model for
666 simulating transient damage-healing processes in self-healing cementitious materials.
667 In *Computational Modelling of Concrete and Concrete Structures*.
668 doi:10.1201/9781003316404-14

669 G., W., & Stroud, A. H. (1973). Approximate Calculation of Multiple Integrals.
670 *Mathematics of Computation*, **27**(122). doi:10.2307/2005635

671 Han, K., Ju, J. W., Zhang, H., Zhu, Y., Chang, T.-S., & Wang, Z. (2021a). Mechanical
672 response analysis of self-healing cementitious composites with microcapsules
673 subjected to tensile loading based on a micromechanical damage-healing model.
674 *Construction and Building Materials*, **280**. doi:10.1016/j.conbuildmat.2021.122251

675 Han, K., Ju, J. W., Zhang, H., Zhu, Y., Chang, T.-S., & Wang, Z. (2021b). Mechanical
676 response analysis of self-healing cementitious composites with microcapsules
677 subjected to tensile loading based on a micromechanical damage-healing model.
678 *Construction and Building Materials*, **280**, 122251.

679 James, G., M., H. M., Tyson, R., Michele, B., Ayman, O., & Somayeh, A. (2014).
680 Dicyclopentadiene and Sodium Silicate Microencapsulation for Self-Healing of
681 Concrete. *Journal of Materials in Civil Engineering*, **26**(5), 886–896.

682 Jefferson, A., & Bennett, T. (2007). Micro-mechanical damage and rough crack closure
683 in cementitious composite materials. *International Journal for Numerical and Analytical*
684 *Methods in Geomechanics*, **31**, 133–146.

685 Jefferson, A. D. (2003). Craft—a plastic-damage-contact model for concrete. I. Model
686 theory and thermodynamic considerations. *International Journal of Solids and*
687 *Structures*, **40**(22), 5973–5999.

688 Jefferson, A. D., & Bennett, T. (2010). A model for cementitious composite materials
689 based on micro-mechanical solutions and damage-contact theory. *Computers &*
690 *Structures*, **88**(23), 1361–1366.

691 Jefferson, A. D., & Freeman, B. L. (2022). A crack-opening-dependent numerical model
692 for self-healing cementitious materials. *International Journal of Solids and Structures*,
693 **244–245**, 111601.

694 Königsberger, M., Pichler, B., & Hellmich, C. (2020). Multiscale poro-elasticity of
695 densifying calcium-silicate hydrates in cement paste: An experimentally validated

696 continuum micromechanics approach. *International Journal of Engineering Science*,
697 **147**, 103196.

698 Krajcinovic, D. (1996). *Damage mechanics*, Elsevier.

699 Lee, F. B., & Anthony, J. (2023). A 3D Coupled Finite-Element Model for Simulating
700 Mechanical Regain in Self-Healing Cementitious Materials. *Journal of Engineering*
701 *Mechanics*, **149**(7), 04023038.

702 Mergheim, J., & Steinmann, P. (2013). Phenomenological modelling of self-healing
703 polymers based on integrated healing agents. *Computational Mechanics*, **52**(3).
704 doi:10.1007/s00466-013-0840-0

705 Mihai, I. C., & Jefferson, A. D. (2011). A material model for cementitious composite
706 materials with an exterior point Eshelby microcrack initiation criterion. *International*
707 *Journal of Solids and Structures*, **48**(24), 3312–3325.

708 Monchiet, V., Gruescu, C., Cazacu, O., & Kondo, D. (2012). A micromechanical approach
709 of crack-induced damage in orthotropic media: Application to a brittle matrix
710 composite. *Engineering Fracture Mechanics*, **83**, 40–53.

711 Oucif, C., & Mauludin, L. M. (2018). Continuum damage-healing and super healing
712 mechanics in brittle materials: A state-of-the-art reviews. *Applied Sciences*
713 *(Switzerland)*. doi:10.3390/app8122350

714 Pensée, V., Kondo, D., & Dormieux, L. (2002). Micromechanical Analysis of Anisotropic
715 Damage in Brittle Materials. *Journal of Engineering Mechanics-Asce - J ENG MECH-ASCE*,
716 **128**. doi:10.1061/(ASCE)0733-9399(2002)128:8(889)

717 Pichler, B., & Hellmich, C. (2011). Upscaling Quasi-Brittle Strength of Cement Paste and
718 Mortar: A Multi-Scale Engineering Mechanics Model. *Cement and Concrete Research*,
719 **41**, 467–476.

720 Pichler, B., Hellmich, C., A. Mang, H., & Aaaa, A. (2007). A combined fracture-
721 micromechanics model for tensile strain-softening in brittle materials, based on
722 propagation of interacting microcracks. *International Journal for Numerical and*
723 *Analytical Methods in Geomechanics*, **31**(2), 111–132.

724 Pichler, B., Hellmich, C., Eberhardsteiner, J., ... Chanvillard, G. (2013). Effect of gel–space
725 ratio and microstructure on strength of hydrating cementitious materials: An
726 engineering micromechanics approach. *Cement and Concrete Research*, **45**, 55–68.

727 Ponnusami, S. A., Krishnasamy, J., Turteltaub, S., & van der Zwaag, S. (2019). A
728 micromechanical fracture analysis to investigate the effect of healing particles on the
729 overall mechanical response of a self-healing particulate composite. *Fatigue and*
730 *Fracture of Engineering Materials and Structures*, **42**(2). doi:10.1111/ffe.12929

731 Sanz-Herrera, J. A., Aliko-Benitez, A., & Fadrique-Contreras, A. M. (2019). Numerical
732 investigation of the coupled mechanical behavior of self-healing materials under cyclic
733 loading. *International Journal of Solids and Structures*, **160**, 232–246.

734 Selvarajoo, T., Davies, R., Freeman, B. and Jefferson, A. (2020). Mechanical response of
735 a vascular self-healing cementitious material system under varying loading
736 conditions. *Construction and Building Materials*, **254**, 119245.
737 ([10.1016/j.conbuildmat.2020.119245](https://doi.org/10.1016/j.conbuildmat.2020.119245))

738 Shields, Y., De Belie, N., Jefferson, A., & Van Tittelboom, K. (2021). A review of vascular
739 networks for self-healing applications. *Smart Materials and Structures*, **30**(6), 063001.

740 Subramanian, H., & Mulay, S. S. (2020). Continuum damage–healing-based constitutive
741 modelling for self-healing materials: application to one-dimensional cyclic loading
742 cases. *International Journal of Advances in Engineering Sciences and Applied
743 Mathematics*, **12**(1–2). doi:10.1007/s12572-020-00266-6

744 Simo J.C., Hughes T.J.R. (1998). Computational Inelasticity. Springer

745 Subramanian, H., & Mulay, S. S. (2022). On the constitutive modelling of elasto-plastic
746 self-healing materials. *International Journal of Solids and Structures*, **234–235**.
747 doi:10.1016/j.ijsolstr.2021.111289

748 Van Tittelboom, K., & De Belie, N. (2013). Self-healing in cementitious materials-a
749 review. *Materials*, **6**(6). doi:10.3390/ma6062182

750 Vermolen, F. J. van Baaren, E. Adam, J. A. (2006). A simplified model for growth factor
751 induced healing of wounds. *Mathematical and Computer Modelling*, **44**(9–10).
752 doi:10.1016/j.mcm.2006.02.017

753 Voyiadjis, G. Z., Shojaei, A., & Li, G. (2011). A thermodynamic consistent damage and
754 healing model for self healing materials. *International Journal of Plasticity*, **27**(7).
755 doi:10.1016/j.ijplas.2010.11.002

756 Zhou, S., Zhu, H., Ju, J. W., Yan, Z., & Chen, Q. (2017). Modeling microcapsule-enabled
757 self-healing cementitious composite materials using discrete element method.
758 *International Journal of Damage Mechanics*, **26**(2). doi:10.1177/1056789516688835

759 Zhou, S., Zhu, H., Yan, Z., Ju, J. W., & Zhang, L. (2016). A micromechanical study of the
760 breakage mechanism of microcapsules in concrete using PFC2D. *Construction and*
761 *Building Materials*, **115**, 452–463.

762 Zhu, C., & Arson, C. (2014). A thermo-mechanical damage model for rock stiffness
763 during anisotropic crack opening and closure. *Acta Geotechnica*, **9**(5), 847–867.

764 Zhu, H., Zhou, S., Yan, Z., Ju, J. W., & Chen, Q. (2015). A two-dimensional
765 micromechanical damage-healing model on microcrack-induced damage for
766 microcapsule-enabled self-healing cementitious composites under tensile loading.
767 *International Journal of Damage Mechanics*, **24**(1), 95–115.

768 Zhu, H., Zhou, S., Yan, Z., Ju, J. W., & Chen, Q. (2016). A two-dimensional
769 micromechanical damage–healing model on microcrack-induced damage for
770 microcapsule-enabled self-healing cementitious composites under compressive
771 loading. *International Journal of Damage Mechanics*, **25**(5), 727–749.

772

773